UCLouvain

École polytechnique de Louvain

Determination of the surface charge density of a nanoporous silicon membrane during electroosmotic pumping

Author : **Laura Dubus**
Supervisor : **Laurent Francis**
Readers : **Wim De Malsche, Romain Hanus, Tristan Gilet**
Academic year 2022–2023
Master [120] in Chemical and Materials Engineering

ABSTRACT

The surface charge density of a porous membrane plays a crucial role in the functioning of an electroosmotic pump. This parameter allows the determination of the flow performance of the pump. This study is dedicated to determining this crucial value for membranes of diverse materials and geometrical characteristics. This determination is achieved through a combination of experimental, analytical and numerical methods, using the Comsol Multiphysics software. The investigation reveals that the highest flow rate, and consequently the maximum surface charge density, is attained by a polycarbonate membrane with a pore size of 3 μm, and is equal to 17.5 μL/min experimentally. Furthermore, the research introduces two surface modifications applied to polycarbonate membranes. An atomic layer deposition of alumina results in a 10% reduction in pore size, remarkably increasing the electroosmotic flow rate by 30% and inducing a reversal in flow direction. Additionally, the deposition of gold on one side of a polycarbonate membrane leads to a substantial 1.85-fold increase in electroosmotic flow rate.

ACKNOWLEDGEMENTS

My sincere thanks to Prof. Laurent Francis, my supervisor, for his valuable guidance and expertise, which significantly contributed to my progress throughout this year.

I'm very grateful to Romain Hanus for his invaluable advice, help and constant availability throughout the year. His dedication and support have been truly appreciated.

I also acknowledge the assistance of Sebastien Faniel and Benjamin Huet from the Winfab cleanroom team, whose help and explanations with the equipment were greatly appreciated.

A great thanks to Laurence Ryelandt for her explanation about the EDX technology and helping me identify the composition of an unkown phenomenon.

I would also like to thank Prof. Wim De Malsche and Tristan Gilet for agreeing to be a member of my Master's thesis jury.

Lastly, I am deeply grateful for the constant encouragement from my family and friends. A particular thanks to my sister for her meticulous proofreading of this thesis and to Sophie Alicandro for her constant support throughout this year.

CONTENTS

LIST OF ACRONYMS

ALD Atomic layer deposition

CDFT Classical density functional theory

EDL Electrical double layer

EDX Energy-dispersive X-ray

EO Electroosmotic

EOF Electroosmotic flow

EOP Electroosmotic pump

HF Hydrofluoric acid

HPLC High performance liquid chromatography

LOC Lab-on-chip

PC Polycarbonate

PET Polyethylene

PI Polyimide

PSi Porous silicon

PZC Point of zero charges

SEM Scanning electron microscope

CHAPTER 1

INTRODUCTION

Electroosmosis, an electrokinetic phenomenon discovered by Reuss in 1809 [1], involves the propulsion of a fluid through capillaries via an externally applied electric field. The first electroosmotic pumps (EOP) were developed in the 1990s, leading to a diverse range of materials being employed to induce this phenomenon.

EOPs offer several advantages. They produce a continuous, pulse-free flow and allow straightforward control of flow rate and direction. Moreover, EOP have no moving parts. Additionally, these pumps can be fabricated using standard microfabrication techniques, making them compatible with lab-on-chip (LOC) devices [2].

Furthermore, EOP have been used in various fields such as high performance liquid chromatography (HPLC) separations [3][4], LOC systems [5][6], microelectronic equipment cooling [7], drug delivery [8], etc. Due to its important use in these fields, it it important to be able to quantify the performance of an EOP.

Therefore, the primary goal of this master's thesis is to determine the performance of an EOP by evaluating the surface charge density of its membrane made of porous silicon. Along with this objective, parameters as pore size or material which impact surface charge density are studied through both experimental and numerical approaches. Notably, membranes with pore size ranging from 150 nm to 3 μm are analyzed, encompassing diverse materials such as polymers and alumina.

Furthermore, to reproduce as closely as possible the characteristics of the porous silicon membrane, two surface modifications are performed on polymer membranes. These modifications include atomic layer deposition to reduce pore size and metallization to enhance the experimental flow rate.

The structure of this master's thesis is as follow. First, a literature review about the main used concepts is done. It begins by presenting a comprehensive review of the core principle of electroosmosis. An overview of the use of porous silicon in electroosmotic pumps is presented, along with a discussion of some of the pumps available in the literature. Moreover, some methods available for determining the surface charge density of silicon surfaces are demonstrates. Secondly, all material used as membranes for EOP for this study as well as their fabrication process are presented. The methods used in this work as the setup for the EOP or some analysis tools are also reviewed. Thirdly, the electroosmosis phenomenon is studied numerically with the software Comsol Multiphysics. Finally, experimental results obtained with the EOP are summarized and discussed.

CHAPTER 2

LITERATURE REVIEW

This chapter begins with a literature review on electroosmotic pumping, providing a comprehensive overview of the topic. It then focuses on electroosmotic pumping for membranes in porous silicon. Additionally, an overview of existing methods used to determine surface charge density of silica surfaces is presented.

2.1 Elecroosmotic pumping

This section firstly describes the phenomenon of electroosmosis and its origin, based on the Gouy-Chapman model of the electrical double layer (EDL). Secondly, the potential variation in the double layer is analyzed. The electroosmotic flow profile in a channel is then described at two different scales: in a microchannel and in a nanochannel.

2.1.1 Electroosmosis phenomenon

Electroosmosis is a phenomenon occurring when an electrolyte contained in a microchannel is subjected to an electric field. This results in the movement of the fluid, as shown in Figure 2.1. This phenomenon was discovered by F. Reuss at the beginning of the 19^{th} century [1].

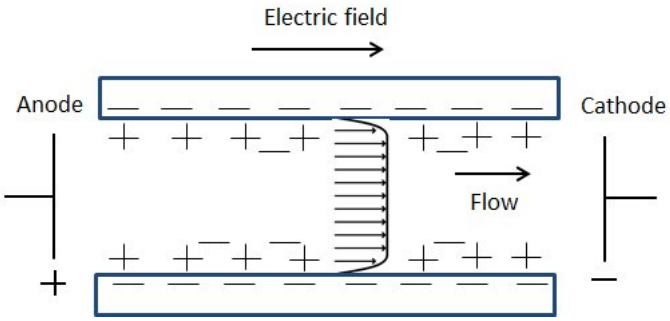

Figure 2.1: Electroosmotic flow in a capillary tube. Figure taken from [9]

Origin of surface charges

As shown in Figure 2.1, surface charges at the interface between the solid and the solution are needed to induce the electroosmosis phenomenon. Most materials obtain surface electric charges when they are brought into contact with an aqueous solution. These surface electric charges can have various origins, as mentioned in [10][11].

The first origin is linked to the affinities of surface ion with the two immiscible phases. Theses affinities are due to physical adsorption (e.g., van der Waals attraction), chemical adsorption (e.g., covalent bonding), or electrostatic attraction.

The second origin is related to the solubility of a solid in an aqueous solution. There is dissolution of one type of ions over the other at the surface of the solid until the product of ionic concentrations equals the solubility product [1]. This dissolution induces the presence of ions at the solid's surface.

The last origin is linked to the ionization of surface groups of the solid. If there is an acidic group at the surface of the solid, it undergoes a dissociation and the surface is negatively charged. For example, a COOH carboxyl group on the surface dissociates in COO^- on the surface and in H^+ in the solution. On the contrary, if the surface contains basic groups, the dissociation of it results in a positively charged surface. In both cases, the solution's pH also influences this phenomenon. Surfaces containing acidic groups have a reduction in surface charges by decreasing pH, and conversely for surfaces containing basic groups.

[1]The solubility product, Ks, of an ionic compound is defined as the product of the concentration of the ions that exist in equilibrium with the solid compound in a saturated solution [12].

Flow of charges

Due to the appearance of surface charges at the interface between the solid and the solution, a movement of the fluid is induced. Under the application of an electric field, a flow of ions migrates towards one of the electrodes, inducing the movement of the fluid. Actually, these ions are accelerated under the effect of the electric field. Due to viscous bonds between these charges and the liquid's molecules, the fluid is driven. Therefore, the ionic charges near the surface of the solid are responsible for the fluid's movement. The disposition of these surface charges can be described with the model of the electrical double layer explained in the following section.

2.1.2 Electrical double layer model

The most known model of the electrical double layer (EDL) is the model of Gouy-Chapman-Stern. It describes the EDL with two different layers: one inner where the ions in the solution are strongly bounded to the solid surface and one outer where they are less firmly attached and can diffuse. This structure can be observed in Figure 2.2.

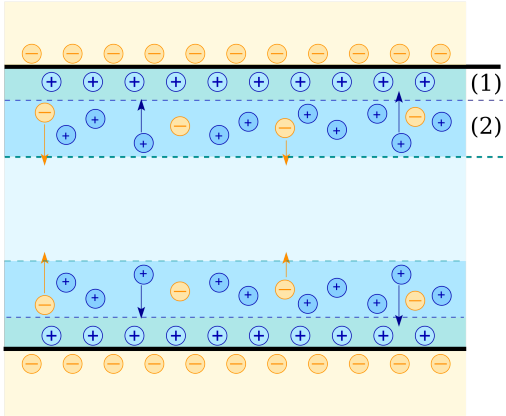

Figure 2.2: Double layer model representation. (1) Stern layer. (2) Gouy-Chapman layer, also called diffuse layer. Figure taken from [13]

The inner layer is called the Stern layer. It is only charged with the ions of opposite charge in relation to the solid. Its thickness is of the order of the molecular diameter, i.e. about several Angstroms. This layer is assumed fixed, the ions are therefore motionless and do not participate to the motion of the electroosmotic (EO) flow.

The second layer in this model is the diffuse layer, also called the Gouy-Chapman layer. The number of counterions in this layer decreases with distance from the surface, while the number of co-ions tends to increase. This layer is the one that participates to the motion of the fluid when an electric field is applied, as the ions it contains are not fixed.

The electrical double layer has a certain thickness. Indeed, when the solid surface charges attracts the electrolyte counter-ions, there is an accumulation of charges at the surface of the solid. This induces a concentration gradient of counter ions in the electrolyte. It is the competition between the electrical attraction of the counter-ions at the surface and the diffusion of these ions in the electrolyte that gives rise to the thickness of the EDL. This thickness is considered to be of the Debye length, which is defined in the literature as:

$$\lambda_D = \sqrt{\frac{\varepsilon k_B T}{\sum_i q_i^2 c_i^0}} \tag{2.1}$$

where $\varepsilon = \varepsilon_0 \varepsilon_r$ is the dielectric permittivity of the solution with ε_0 and ε_r the vacuum electrical permittivity, and the solution's relative permittivity with respect to vacuum, respectively; T is the temperature of the solution, k_B is the Boltzmann constant, and c_i^0 is the concentration of ions of charge q_i away from the shielded charge, where the electric field is zero [14]. The value of the Debye length mainly depends on the bulk ionic concentration. For example, in KCl solutions, when the molar concentration is 10^{-6} M, the Debye length is equal to 304 nm. When the concentration is higher, equal to 10^{-4} M, $\lambda_D = 30.4$ nm, which is relatively smaller [11].

2.1.3 Potential inside the double layer

The distribution of charges in the electrolyte creates an electric potential. This potential, denoted Ψ, can be described by the Poisson equation for the Gouy-Chapman model:

$$\nabla^2 \Psi = -\frac{\rho_e}{\varepsilon} = \frac{-eN_A}{\varepsilon} \sum_{i=1}^{m} z_i c_i \tag{2.2}$$

ρ_e is the total charge density, e is the elementary charge, N_A is the Avogadro's number, ε is the dielectric permittivity of the solution, z_i is the the valence and c_i is the bulk ion concentration [15]. Because there are ionic species in solution that feels the local electrostatic potential from the charged solid–liquid interface, the Boltzmann equation can be introduced to have a better approximation of the

model used. In this case, the potential Ψ can be found with the following equation [16], called the Poisson-Boltzmann equation:

$$\varepsilon(\nabla^2\Psi) = 2ec_i\sinh\left(\frac{e\Psi}{k_BT}\right) \tag{2.3}$$

The maximum value of the electrical potential in the double layer is at the surface of the channel, where the charged ions are adsorbed, as shown in Figure 2.3. The potential then linearly decreases to the end of the Stern layer. From this point, the potential decreases exponentially with the distance from the walls, until it reaches the shear plane. This plane is a boundary in the diffuse layer that separates ions that forms an entity with the particle and the ones that are not. When a particle moves, ions within the boundary move with it while the ones beyond the shear plane stay with the bulk. At the shear plane, the internal potential reaches a value called "zeta potential (ζ)". Finally, far away from the surface of the channel, the potential is considered to be zero.

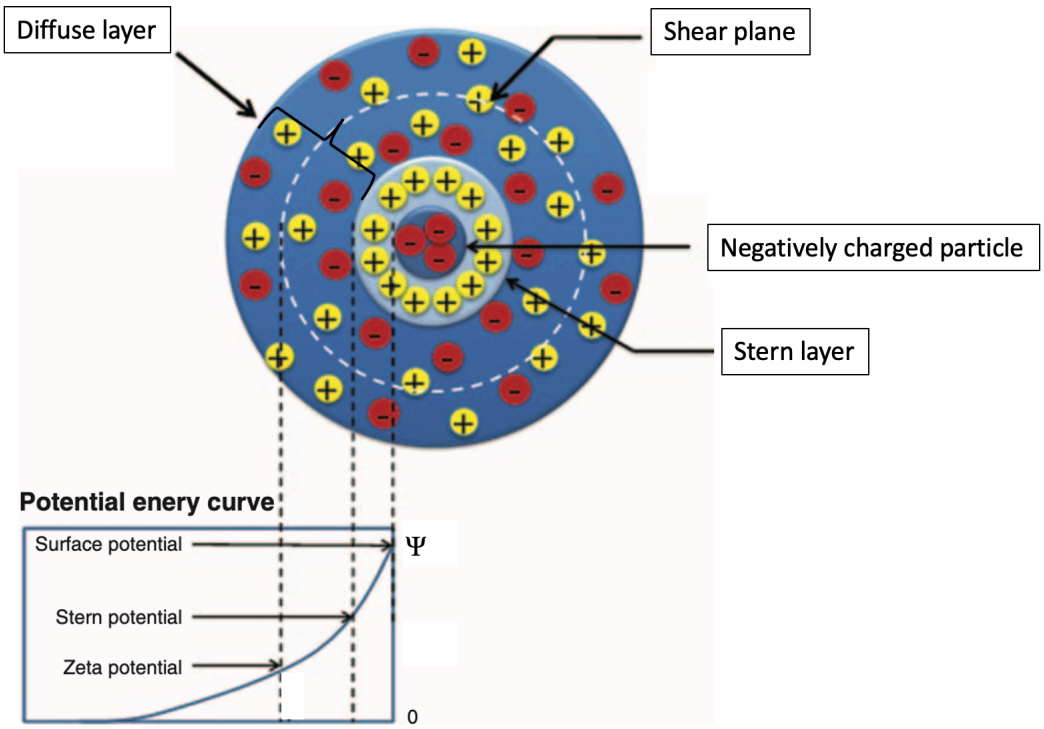

Figure 2.3: Potential variation inside the electrical double layer. Figure modified from [17].

The zeta potential is an important value in the electrical double layer. It allows knowing the total charge density at the shear plane, thus the quantity of ions that

participates in the fluid's movement. The zeta potential can be found knowing the surface charge density σ at the interface with the channel:

$$\zeta = \frac{\sigma \lambda_D}{\varepsilon} \tag{2.4}$$

In addition to the parameters described in equation 2.4, zeta potential is also influenced by the pH of the solution. When decreasing the pH, ζ increases and conversely. Additionally, there exists a pH where zeta potential is equal to zero. It is called the isoelectric point [18]. . Moreover, ζ also varies with the ionic concentration of the electrolyte. The potential decreases with increasing concentration, as it is related to the Debye length.

2.1.4 Electroosmotic flow

In a straight microchannel

The profile of the electroosmotic flow in a straight microchannel is shown in the upper part of Figure 2.4. As mentioned previously, the flow is driven by the movement of ions in the electrical double layer. In a large capillary, thus when the radius of the capillary is considered sufficiently large compared to Debye length, the flow is considered to be flat. To have a flow of this type, some assumptions are made. Firstly, the flow at the interface between solid and liquid is null because of the non-slip condition. Secondly, the hydrodynamic resistance of the fluid is neglected. In this case, the electroosmotic velocity is given by:

$$u_{EOF}(y) = -\frac{\varepsilon E_x}{\mu}\zeta \tag{2.5}$$

where ε is the dielectric permittivity of the solution, E_x is the external electric field in the axial direction and μ is the fluid's viscosity.

The total velocity of the fluid is also influenced by the pressure-driven flow. This flow is shown in the middle of Figure 2.4. Consequently, the net flow is the sum of the electroosmotic flow and the pressure-driven flow. This is shown in the lower part of Figure 2.4.

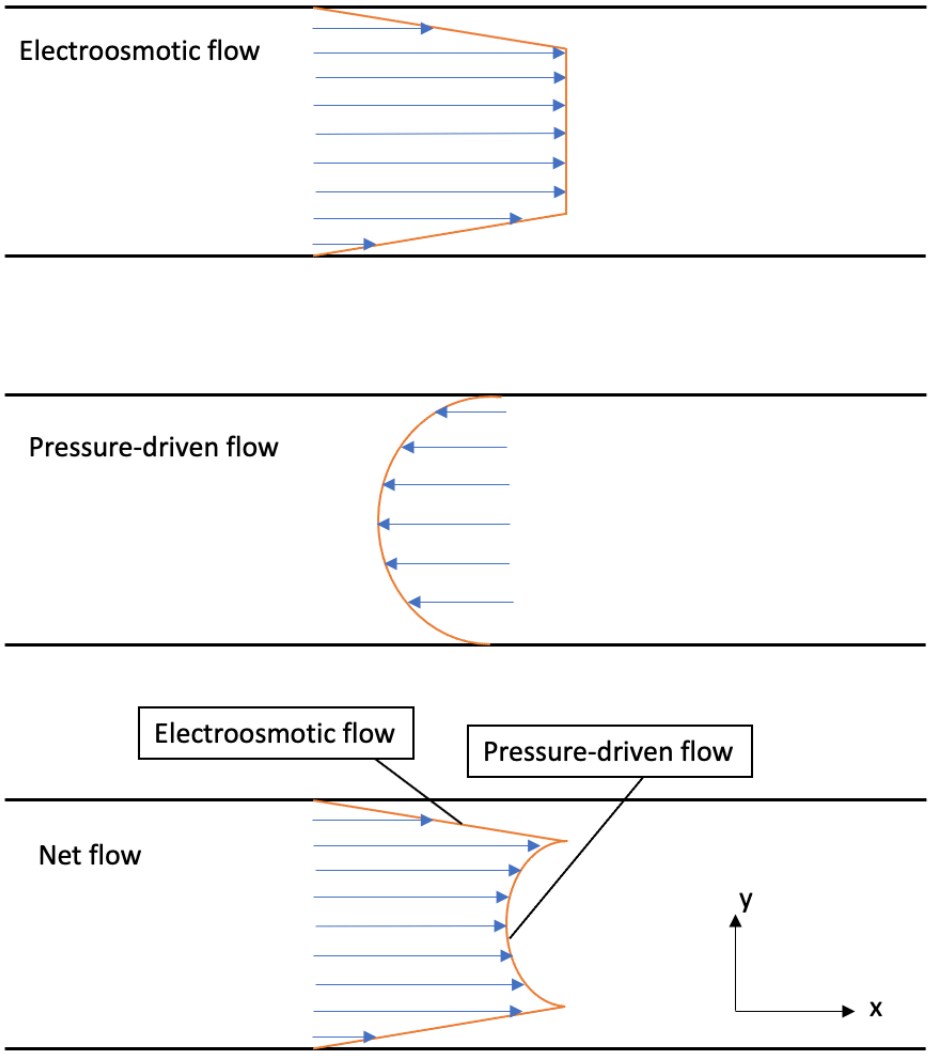

Figure 2.4: Flow profile in a straight microchannel, with the contribution of electroosmotic and pressure-driven flow.

In a straight nanochannel

In the case of a nanochannel, the velocity profile is not the same. If the radius of the nanochannel is smaller or equal to the Debye length, there is an overlap of the electrical double layer, as shown in Figure 2.5. Each ion in the fluid thus participates in its movement (except those who are in the Stern layer). This gives a selective property to the channel as the ions flowing through it are mainly composed of one type of ions, the counterions of the channel's surface.

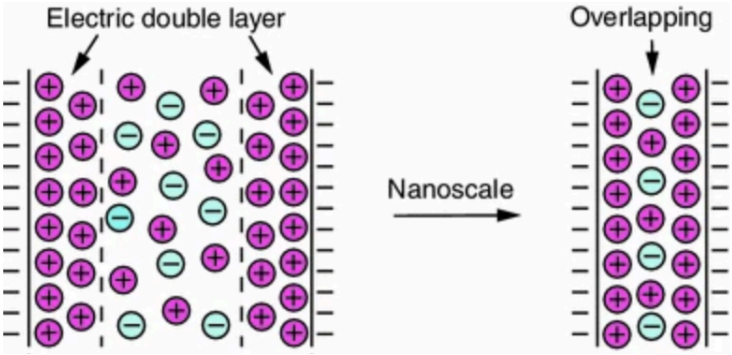

Figure 2.5: Nanoscale EDL overlap. Figure modified from [19].

Ran Peng and Dongqing Li have studied this phenomenon in [20]. They found that in relatively large nanochannels (over 100 nm), for a 10^{-3} M solution, the electroosmotic flow (EOF) velocity is around 43 μm/s and is independent of channel size. On the contrary, when the channel size is less than 100 nm, for the same concentration, the EOF velocity becomes size-dependent and decreases with channel size. In fact, for a 10^{-3} M solution, the Debye length is around 30-50 nm. Consequently, channels smaller than 100 nm are likely to have an overlapping of their EDL in a solution of the same concentration.

The total fluid's velocity in a nanochannel is given by [16]:

$$u(y) = \frac{-P}{2\mu}(y^2 - 2hy) + \frac{E_x\varepsilon}{\mu}(\Psi(y) - \zeta) \tag{2.6}$$

where $P = \frac{-dp}{dx}$ is the applied pressure gradient. This equation shows that the velocity is a result of the pressure-driven flow and the electroosmotic flow, as in a microchannel. Therefore, the electroosmotic flow is given when $P = 0$ and is:

$$u_{EOF}(y) = \frac{E_x\varepsilon}{\mu}(\Psi(y) - \zeta) \tag{2.7}$$

This profile is shown in Figure 2.6. In this case, it is only curved [16].

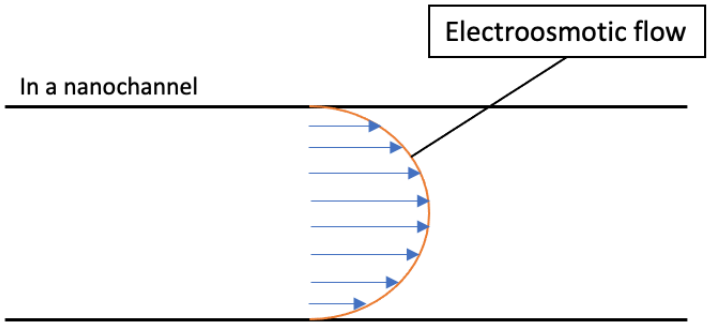

Figure 2.6: Electroosmotic flow profile in a nanochannel.

2.2 Porous silicon membranes for electroosmotic pumps

As previously mentioned, the objective of electroosmotic pumping is to generate fluid movement by applying an electric field to an electrolyte contained in a channel. In this way, the larger the liquid/solid interface in the pump, the stronger the fluid movement. For this reason, porous materials are ideal candidates for electroosmotic pumping.

In addition, the upcoming sections of this literature review will focus on studying porous silicon. This choice is motivated by the fact that this work is part of a doctoral thesis at UCLouvain focusing, among other things, on the characterization of porous silicon for reverse electrodialysis (RED). Consequently, the aim of this study is related to electroosmotic pumping with porous silicon (PSi).

2.2.1 Characteristics of PSi

Porous silicon was discovered by Arthur Uhlir Jr. and Ingeborg Uhlir in 1956 by electrochemical dissolution of silicon wafers in hydrofluoric acid (HF) [21]. Nevertheless, interest in PSi really exploded in the years 1990 when Leigh Canham published his results. He confirmed that the material could exhibit efficient, bright red-orange photoluminescence. Since that time, a lot of research on PSi has been made because of its characteristics. It has excellent thermal and mechanical properties, it has a large surface area within a small volume (up to 800 m^2/g) [22], controllable pore size, interesting optical properties, it is low cost, etc. All this characteristics makes PSi a excellent material for a lot of applications like optical sensing applications, biomedical applications and electronics [21][23].

2.2.2 Reaction of PSi with the electrolyte

In an electroosmotic pump, the membrane made of porous silicon is immersed in an electrolyte. This effect creates an electrical double layer in the system, as explained in section 2.1.1. In the case of porous silicon, it undergoes an ionization of the surface SiOH group. This can be done two ways: the membrane can undergo either protonation or deprotonation, depending on the pH of the solution. If the pH of the solution is lower than the point of zero charges (PZC), SiOH becomes SiO^-. The membrane thus becomes negatively charged and the positive ions of the electrolyte are attracted. Therefore, the membrane is permeable to the cations. This phenomenon is shown in Figure 2.7. Conversely, if the pH of the solution is higher than the PZC, SiOH becomes $SiOH_2^+$. In that case, the membrane is permeable to anions. Moreover, if the pH of the solution is the neutral pH of the PSi, thus between 3.4 and 4.4 [24], the oxide is at the point of zero charges. In that case, the net surface charges are null.

Figure 2.7: Ion exchange in a porous silicon membrane immersed in a solution with a pH lower than the zero point of charges.

2.2.3 Existing PSi electroosmotic pumps

Various electroosmotic pumps dealing with porous silicon can be found in literature, with different geometries and experimental conditions. In order to compare the maximum generated flow rate for pumps of various geometries and voltages, a flow rate normalized by the voltage and the surface in contact with the electrolyte expressed in $\mu L/(min\ cm^2 V)$ is used by scientists. Theses pumps can be found in table 2.1.

Table 2.1: Table of performance in terms of maximum normalized flow rate of electroosmotic pumps made of porous silicon membranes in the literature.

Article		[25]	[26]	[27]	[28]
Pore size	[μm]	3	3.6	19.5 *10^{-3}	2.3 * 10^{-3}
Effective area	[cm^2]	1	0.07	36 * 10^{-4}	1.89 * 10^{-5}
Pore density	%	45	37.8	5.7	16.7
Thickness	[μm]	350	500	0.015	0.075
Tension	[V]	25	60	20	1
Distance between 2 electrodes	[mm]	2	3	/	4
Electrolyte		10^{-3}M NaCl	DI water	0.1M KCl	0.4M KCl
Maximum flow rate	$[\frac{\mu L}{min\ cm^2 V}]$	128	19.8	138.9	10.72 *10^3

When examining the table, two distinct categories of electroosmotic pumps can be distinguished: those with ultra-thin membranes, and others with significantly thicker membranes. In references [27] and [28], the membranes thickness are reported to be respectively of 15 nm and 75 nm. These values are four orders of magnitude smaller than those of the first two EOP in the table above. As flow rate is inversely proportional to membrane thickness, decreasing the thickness by a factor of 1000 has a substantial impact on the flow performance of the pump.

As mentioned earlier, the flow rate is normalized to μL/(min cm^2V) for comparing different pump performances. However, this normalization does not consider two important parameters. Firstly, the applied voltage is taken into account but without considering the distance between the two electrodes, which determines the induced electric field. As the distance between the electrodes increases, the induced electric field decreases, resulting in a lower flow rate. Secondly, the membrane thickness, as discussed previously, also affects the flow rate but it is not considered in this standardization. Therefore, particular attention should also be paid to these two parameters influencing the flow performance when comparing various EOP.

2.3 Surface charge density

Surface charge density governs ion transport through the pores of the PSi membranes as it is the density of charges that participates to the movement of the fluid. If this density is high, the electroosmotic flow is high and conversely. Determining surface charge density of porous silicon membranes is very important in

this work because knowing this value enables us to calculate the efficiency of the electroosmotic pump in terms of flow rate.

2.3.1 Surface charge density of silica nanospheres

Ya-Rong Shi et al. studied in [29] a way to determine the surface charge density of silica particles in a NaCl solution, by converting their corresponding measured zeta potential with the Poisson Boltzmann model. In this model, the particle size is explicitly included with the radius a of the particle. The surface charge density can be approximated by:

$$\sigma = \frac{2\varepsilon_0\varepsilon_r\kappa RT}{F} sinh\left(\frac{zF\zeta}{2RT}\right)\left\{1 + \frac{2}{\kappa a}\left[cosh\left(\frac{zF\zeta}{4RT}\right)\right]^{-2} + \frac{16}{(\kappa a)^2} ln\left(\left[cosh\left(\frac{zF\zeta}{4RT}\right)\right]\left[sinh\left(\frac{zF\zeta}{2RT}\right)\right]\right)^{-2}\right\}^{1/2} \quad (2.8)$$

In this equation, ε_0 and ε_r are respectively the permittivity of vacuum and the solution's relative permittivity, κ is the reverse of the Debye length, R is the universal gas constant, T is the temperature, F is the Faraday constant, ζ is the zeta potential, and z is considered to be equal to one.

This equation was solved by the same authors for nanoparticles of different sizes. The study reveals that surface charge density decreases as particle size increases, and almost reaches a stable value from a critical particle size. Therefore, it shows that nanoparticle curvature clearly has an effect on surface charge density.

2.3.2 Surface charge density of silica nanopores

Li-Hsien Yeh et al. studied a way in [30] to determine the surface charge density in silica nanopores. Jie Yang et al. used a similar method in their paper [31]. In both cases, they used the full multi-ion surface charge-regulation model that consists in using two concepts simultaneously: the classical density functional theory and the surface reaction model.

Classical density functional theory (CDFT)

This theory describes the electrical double layer as explained in chapter 2.1.2. The mean electric potential is described by the Poisson equation for the Gouy-

Chapmann model and is related to the local charge density by the equation:

$$\nabla^2\Psi(z) = -\frac{\rho_e}{\varepsilon} = \frac{-e}{\varepsilon_0\varepsilon_r}\sum_{i=1}^{m} z_i c_i(z) \tag{2.9}$$

where z_i is the valence of ionic species i and $c_i(z)$ is the ionic density distribution inside the pore. The following boundary conditions are applied, where D is the width of the pore:

$$\Psi(0) = \Psi(D) = \Psi_0 \tag{2.10}$$

CDFT theory also predicts that the ionic density distributions inside the pores are given by:

$$c_i(z) = c_i^0 \exp[-\beta V_i(z) - \beta z_i e\Psi(z) - \beta\Delta\mu_i^{ex}(z)] \tag{2.11}$$

where $V_i(z)$ is the wall potential, $\beta = 1/(k_B T)$, k_B is the Boltzmann constant and $\Delta\mu_i^{ex}(z)$ accounts for the electrostatic correlations and ionic excluded volume effects. These equations can be solve numerically. From equations 2.9 and 2.11, it is possible to calculate the surface charge density σ according to the overall charge neutrality condition:

$$\sigma = -\sum_i z_i e \int_0^{L/2} c_i(z)dz \tag{2.12}$$

where L denotes the pore length.

Surface reaction model

The surface charge density σ can be found by the surface reaction model. Charge regulation takes place at the solid/liquid interface where protonation and deprotonation reactions occur, as explained in section 2.2. Two main associations/dissociation reaction happen on that silica interface:

$$\mathrm{SiOH} \longleftrightarrow \mathrm{SiO^-} + \mathrm{H^+} \qquad \{1\}$$

$$\mathrm{SiOH} + \mathrm{H^+} \longleftrightarrow \mathrm{SiOH_2^+} \qquad \{2\}$$

with the respective equilibrium constants K_A and K_B:

$$K_A = \frac{N_{SiO^-}[H^+]_s}{N_{SiOH}} \tag{2.13}$$

$$K_B = \frac{N_{SiOH_2^+}}{N_{SiOH}[H^+]_s} \tag{2.14}$$

In the above, N_{SiO^-}, $N_{SiOH_2^+}$ and N_{SiOH} are the surface densities of SiO^-, $SiOH_2^+$ and SiOH respectively. $[H^+]_s$ is the concentrations of H^+ ions at the silica interface. It follows the Boltzmann distribution, such as:

$$[H^+]_s = [H^+]_0 \exp\left(\frac{F\zeta}{RT}\right) \tag{2.15}$$

where F denotes the Faraday constant. The total number density of SiOH molecules on the solid liquid interface is given by three contributions:

$$N_{tot} = N_{SiO^-} + N_{SiOH_2^+} + N_{SiOH} \tag{2.16}$$

Finally, from theses equations, the surface charge density of the silica nanopore can be obtained by:

$$\begin{aligned} \sigma &= F(N_{SiOH_2^+} - N_{SiO^-}) \\ &= -FN_{tot}\frac{K_A - K_B\left([H^+]_0 \exp\left(\frac{F\zeta}{RT}\right)\right)^2}{K_A + [H^+]_0 \exp\left(\frac{F\zeta}{RT}\right) + K_B\left([H^+]_0 \exp\left(\frac{F\zeta}{RT}\right)\right)^2} \end{aligned} \tag{2.17}$$

2.3.3 Parameters affecting surface charge density

Three main parameters are affecting surface charge density for porous silicon: the pH of the solution, the salt concentration in the solution and the particle size, as described in [30][29][32].

Firstly, when the particle size decreases, the surface charge density tends to increase. This is due to the decrease in the surface concentration of H^+ ions, leading to a higher proportion of negatively charged SiO^- dissociated from the functional groups SiOH. As a result, the surface becomes more negatively charged, increasing the surface charge density. However, there is a critical particle size below which the surface charge density becomes independent of the particle size. Once the particle size reaches this critical diameter, further reductions in size have little effect on the surface charge density, and it stabilizes at a certain level depending on the pH and salt conditions of the solution.

Secondly, the salt concentration of the solution also affects surface charge density. With a fixed particle size, the increased background salt concentration attracts more K^+ ions to the negatively charged particle surface. As a result, the higher concentration of K^+ ions excludes H^+ ions from the surface, leading to a lower concentration of H^+ ions on the particle surface. This decrease in H^+ ions results in a higher negative surface charge density, as more negative charges remain on the surface.

Finally, the surface charge density of particles increases as the pH of the solution decreases. In acidic conditions, there is a higher concentration of H^+ ions in the solution. As a result, more of these H^+ ions interact with the functional groups on the silica surface, leading to a higher degree of protonation. This increased protonation results in a higher positive surface charge density.

2.4 Objectives of this master's thesis

The literature contains several articles that demonstrates the feasibility of using porous silicon as the membrane material in an electroosmotic pump. Furthermore, equation 2.5 and 2.6 allow the calculation of the EOF in a microchannel and in a nanochannel considering various parameters, including the zeta potential. Therefore, by observing the flow rate obtained during electroosmotic pumping, it becomes possible to determine the zeta potential of a porous silicon membrane. Finally, several papers demonstrate the possibility of analytically determining the surface charge density of a silicon nanopore.

Therefore, the ultimate goal of this work is to analytically determine the surface charge density of a porous silicon membrane. This can be achieved by experimentally determining the zeta potential through the electroosmotic flow rate measurements and subsequently using this data to calculate the surface charge density. By combining experimental and analytical methods, a comprehensive understanding of the surface properties and behavior of porous silicon membranes in an electroosmotic pump can be achieved.

CHAPTER 3

MATERIALS AND METHODS

This chapter provides a comprehensive overview of the membranes used in electroosmotic pumping for this study. These membranes encompass a range of materials, including polymers and porous silicon. The chapter highlights the diverse techniques employed for manufacturing these membranes and outlines the various surface treatments applied.

Moreover, this chapter provides a thorough explanation of the methodologies employed to acquire the results. It includes a comprehensive description of the experimental setup used in the study. Special emphasis is given to the introduction of specific software tools, such as the Scanning Electron Microscope (SEM) and ImageJ, which played a crucial role in the analysis and interpretation of the acquired data. In addition, a model for analytically determining the flow performance of a pump is presented.

3.1 Materials

3.1.1 Raw membranes

Track etched polymer membranes

Various polymer membranes are used in this work. They vary according to their geometry, differing in pore size and thickness, as well as in material. The membranes used can be made of polycarbonate (PC), polyethylene (PET) or polyimide (PI). These membranes are produced by the technique of track-etching. As shown

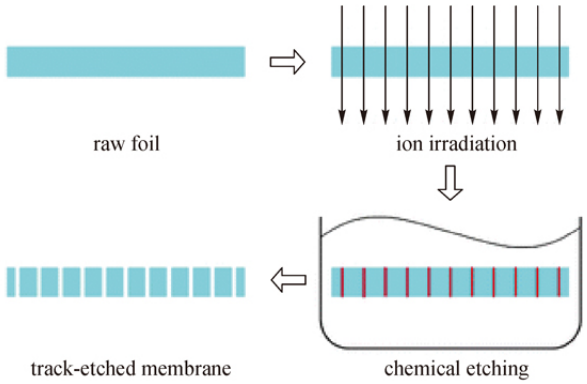

Figure 3.1: Schematic representation of the manufacturing process for a track-etched membrane. Figure taken from [33]

.

in Figure 3.1, this technique consists in firstly irradiating a raw foil of polymer with a beam of energetic heavy ions. The resultant ion tracks are then etched chemically, leading to the track etched membrane [33]. The track etched membranes used in this work are produced by the company it4ip (Ion Track for Innovative Products) in Louvain-la-Neuve in Belgium. An advantage of this technique is that it produces straight pores, benefiting the EO pumping. In this work, the track etched membranes used vary mainly in the polymer composition and in their pore size, ranging from 150 nm to 400 nm of diameter.

Aluminum oxide membrane

Porous aluminum oxide membranes are also used in this work. They are produced by anodic oxidation of aluminum [34]. To manufacture these membranes, an aluminum plate is immersed in an acid solution as the anode, while another electrode acts as the cathode. As a result of the electrolysis reaction, the aluminum is oxidized and nanopores are formed perpendicular to the surface [35].

Porous silicon

The third type of membranes used in this work are the ones in porous silicon. They are formed by etching crystalline silicon in aqueous or non-aqueous electrolytes containing hydrofluoric acid (HF). As shown in Figure 3.2, the surface of a silicon wafer is in contact with a solution containing HF. The silicon wafer acts as the working electrode and a counter electrode, typically in platinum, is immersed in the solution.

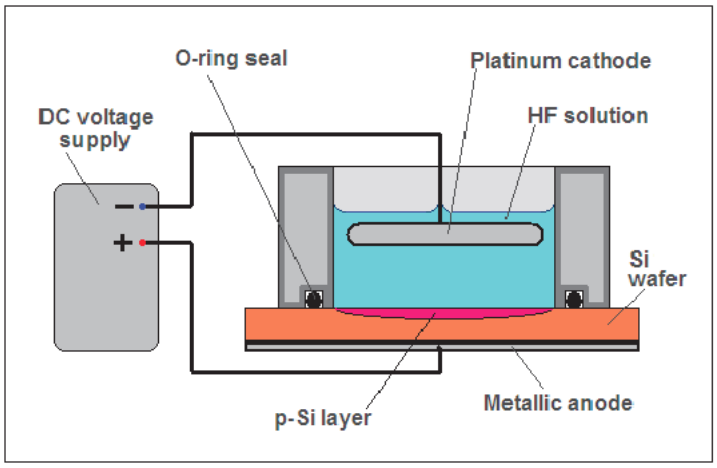

Figure 3.2: Schematic representation of a two-electrode electrochemical cell used to manufacture porous silicon. Figure taken from [36].

Depending on the current density applied to the electrochemical cell, two modes of PSi etching can be reached: the pore formation regime or the electropolishing regime. The dissolution reaction of silicon allowing the formation of pores depends on interaction phenomena at the interface between silicon and the electrolyte of the cell. Indeed, the dissolution of the silicon is initiated when the HF reaches the pore tips and weakens the Si-H surface bonds. Increasing the current density leads to a shrinking of the pores walls, until the pores merge in the electropolishing regime. In this regime, no PSi is formed because it removes silicon atoms uniformly, resulting in a smooth, polished surface. As shown in Figure 3.3, a current-voltage curve can be determined for the electrochemical etching of the silicon. The pore formation regime remains active until the curve reaches its maximum value, at which point the electropolishing regime is activated [23].

In a chemical point of view, pore formation can be expressed with the global semi-reaction that occurs at the surface of the silicon wafer:

$$\mathrm{Si} + 2\,\mathrm{HF} \longrightarrow \mathrm{SiF_2^-} + 2\,\mathrm{H^+} + 2\,\mathrm{e^-} \qquad \{3\}$$

In this reaction, silicon (Si) reacts with hydrofluoric acid (HF) to form negatively charged silicon fluoride ions ($\mathrm{SiF_2^-}$), positively charged hydrogen ions ($\mathrm{H^+}$), and electrons ($\mathrm{e^-}$). The release of these species during the reaction leads to the dissolution of silicon and the formation of pores in the silicon wafer.

The PSi membranes used in this work are produced in a cleanroom facility at UCLouvain. They are manufactured following the process explained above.

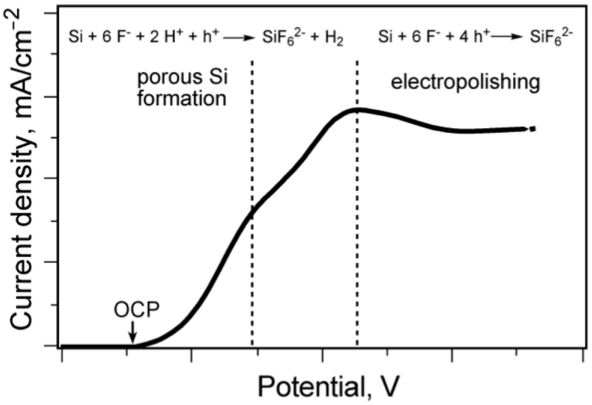

Figure 3.3: Current density versus applied potential curve for electrochemical etch of silicon in an HF electrolyte. Figure taken from [23].

3.1.2 Surface modifications

In this work, two surface modifications are performed on some track etched polycarbonate membranes: atomic layer deposition (ALD) and metallization of one side of the membrane. Both modifications are carried out in the technological platform Winfab, which maintains a cleanroom infrastructure within UCLouvain.

Atomic layer deposition

Atomic layer deposition allows the deposition of ultra-thin films (a few nanometers) in a controlled and precise way. In this work, the process consists in depositing alumina (Al_2O_3) on the whole membrane, so as to cover the internal walls of the pores. This procedure takes place at 100°C by a plasma process. The process can be divided into two half-cycles and is shown in Figure 3.4. In the first half-cycle, a precursor (trimethylaluminum for alumina deposition [37]) is introduced into the reactor and adsorbed onto the substrate surface. Once the surface is saturated, the excess precursor is purged with inert gases. The second half-cycle can then begin. Plasma is pulsed into the chamber, reactivating the membrane surface. The reactor is then purged again, completing the second half-cycle. The ALD process continues by repeating both half-cycles mentioned above for a certain amount of times. Therefore, the number of cycles performed determines the thickness of the deposit [38].

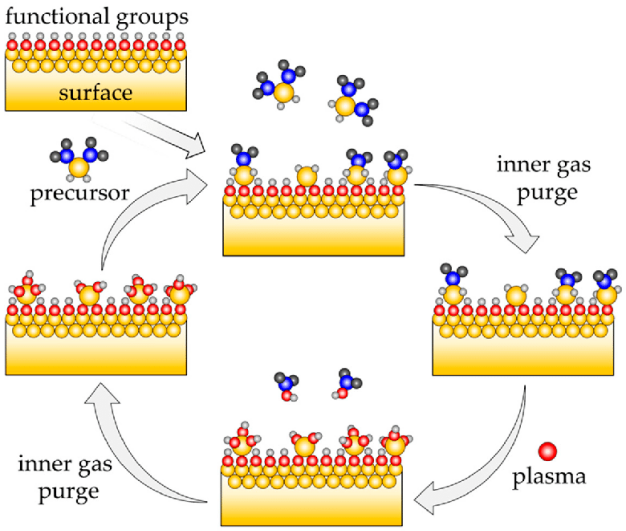

Figure 3.4: Schematic representation of the plasma-enhanced atomic layer deposition process. Figure taken from [38].

The first objective of this surface modification is to reduce the pore size of the membrane. Secondly, depositing another material on the membrane modifies the zeta potential of the electrical double layer. This deposition allows studying the changes in charge density at the surface of the membrane, and consequently its performances. Two different deposits are performed: one of 50 ALD cycles of alumina and another of 200 ALD cycles of the same oxide. The deposits are only performed with Al_2O_3 because it can be used with a plasma-enhanced process and has the highest zeta potential in comparison to the other oxides available in the laboratory [39]. The deposition of this oxide on the membranes is performed using the Cambridge Fiji atomic layer deposition system.

Metal deposition

The second surface modification performed in this work is a metallization of one side of some track etched membranes. For this work, a 5 nm titanium deposit is first deposited as an adhesive layer. A second 50 nm gold deposit is then applied. This metallization is performed by evaporation of the metal by a heating element in a vacuum chamber. The objective of this surface modification is to use the metallized membrane as one of the two electrodes in the electroosmotic pump to enhance the EOF. The distance between the electrodes is thus halved and a higher electric field is normally induced with the same amount of applied tension. The deposition of the gold on the membranes is performed using the E-Gun Vacotec.

3.2 Methods

3.2.1 Electroosmotic pump setup

The experimental electroosmotic pump setup used in this work is shown in Figure 3.5. It was inspired from a previous work done by Jérémie Janssens in [40]. This device was designed with SolidWorks software and machined from a Plexiglas cylinder. The various plans of this setup are given in appendix A of this work. To avoid a pressure effect due to the difference in water level in the two pipettes, this setup must be placed horizontally, so as to observe only the electroosmosis flow. The observation of this flow is done by looking at displacement of the water meniscus in the two graduated pipettes. Each pipette is connected to a reservoir containing the electrolyte, and these are separated by a porous membrane. The contact surface between the membrane and the electrolyte is 29.7 mm^2. To apply some tension in the circuit, two electrodes separated by a distance of 2.4 cm are placed in a way to surround the membrane. These electrodes are rectangular meshes in platinum and have a surface of one square centimeter. The tension in the EO pump is applied with a voltage source, the model 6418 of the brand Keithley. To insert the electrolyte in the device, two tubes are connected to the reservoirs. The liquid is inserted by using a pressure-based flow control device, the LineUp Flow EZ^{TM}. To assure the waterproofing of the setup, the electrodes and the pipettes are inserted in the reservoirs with perforated plugs.

To have a better understanding of the way this experimental electroosmotic pump works, a diagram is presented in Figure 3.6. The tension applied at the electrodes **(1)** induces an electric field in the liquid contained in the reservoirs **(4)**. Due to the properties of the porous membrane **(5)**, an electroosmotic flow is induced through it and it is visible by the changes of volume of the liquid present in the graduated pipettes **(2)**.

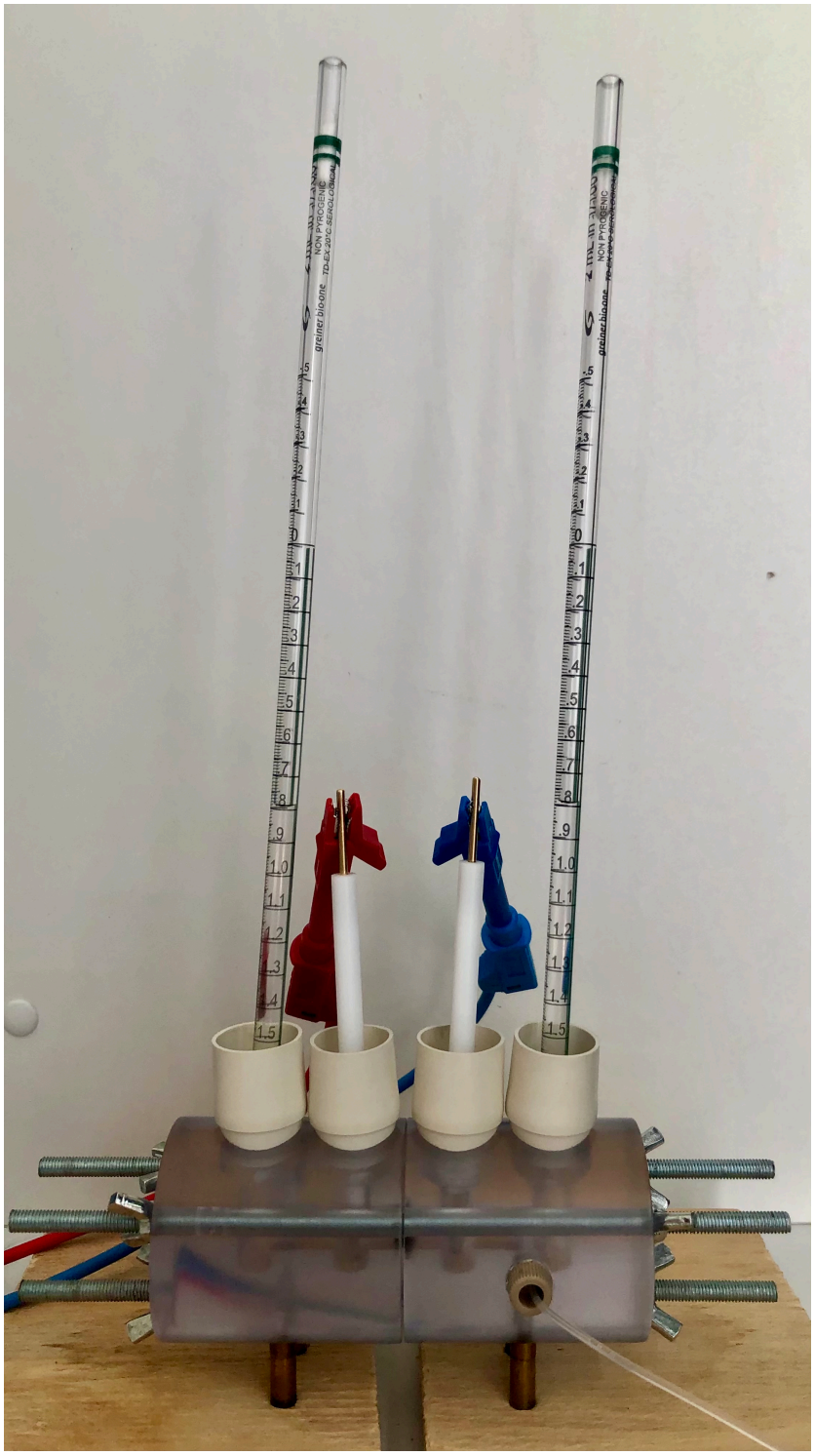

Figure 3.5: Experimental set-up of the EOP.

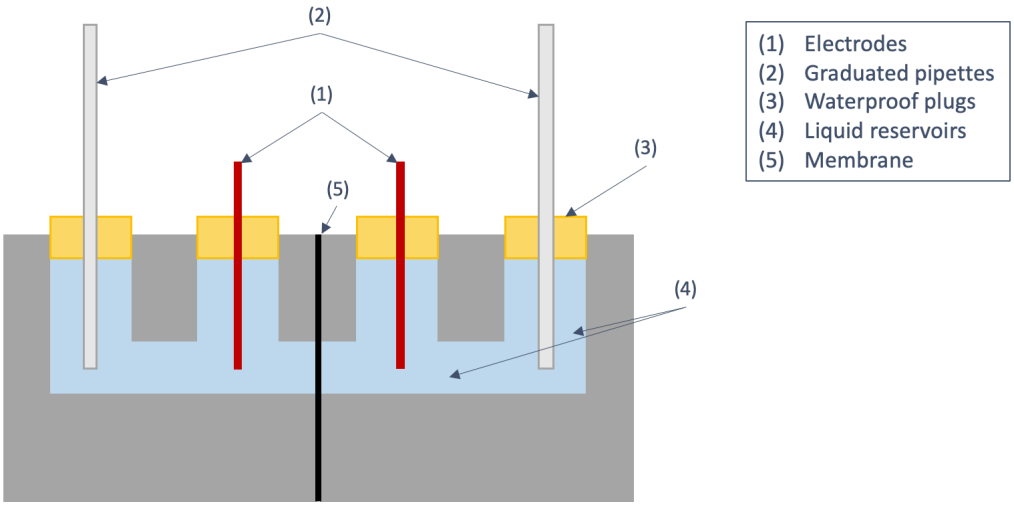

Figure 3.6: Schematic representation of the experimental electroosmotic pump.

3.2.2 Scanning electron microscope

Scanning electron microscopy is an imaging technique that provides high-resolution images of a sample surface. To produce an image, a beam of electrons produced by an electron gun is accelerated along the column of the device. It passes through a series of electromagnetic lenses and apertures that focuses the electron beam. Once this beam hits the sample, a series of electrons (backscattered electrons and secondary electrons) and x-rays are ejected from it. A detector then recognizes these electrons and converts them into a signal that produces the final image [41].

The objective of using a scanning electron microscope in this work is to characterize the various membranes (with and without surface modifications) used for the EO pumping. By obtaining top-view and cross-section images of the membranes, it allows determining the geometric characteristics of it. The SEM used to image the sample is a Zeiss Auriga FIB-SEM, located in the Winfab platform at UCLouvain.

3.2.3 Energy-dispersive X-ray (EDX) spectroscopy

EDX spectroscopy identifies the elemental composition of a sample. As with SEM, an electron beam is projected onto the sample surface to excite it. The difference lies in the detector. In EDX spectroscopy, it's the photons ejected from the sample surface that are of interest. When the surface sample is excited, it dissipates part of the absorbed energy by ejecting a core-shell electron. An outer

shell electron of higher energy then replaces it, releasing an energy gradient in the form of an X-ray, with a characteristic spectrum depending on its atom of origin [42].

The aim of EDX spectroscopy in this work is to identify the elemental composition of the membrane used, in particular to see changes in its composition after being used in the electro-osmotic pump.

3.2.4 ImageJ

Once top-view images of the membranes have been obtained with the SEM, they can be analyzed with ImageJ software. This is used to determine the geometric characteristics of the membranes, such as porosity or pore size. The module used in this software is the "particle analysis" module. This function counts the particles present in the image. For this purpose, the image must be in black and white. To do this, a threshold needs to be set that highlights interesting particles in the background. All image pixel values below the threshold are converted to black and conversely [43].

To count and measure the various particles in the image, the software scans the image until it finds the edge of an object. The surface area of each particle is then found, enabling the total surface area of particles in the image to be determined. This specifies the porosity of the membrane. The software also calculates the Feret diameters of each particle. The minimum Feret diameter corresponds to the shortest distance between any two points on the particle. This result is used to determine the average pore size of the membrane [44].

3.2.5 Analytical model determining pump flow performance

To compare the experimentally obtained flow rate with the theoretical prediction, an analytical model for calculating the flow rate is introduced below.

To determine the efficiency of an electroosmotic pump, the volume flow rate needs to be known. This value can be determined by integrating the electroosmotic flow profile on the section of the channel. For a single cylindrical microchannel, the flow equation is given by [45][46]:

$$u(r) = -\frac{1}{4\pi}(a^2 - r^2)\frac{dP}{dx} - \frac{\varepsilon E}{\mu}(\zeta - \Psi(r)) \tag{3.1}$$

where $\frac{dP}{dx}$ is the pressure gradient, a is the radius of the channel, r is the distance from symmetry axial, $\Psi(r)$ is the radial potential, and E is the strength of the

electric field. Knowing this equation allows the determination of the volume flow rate for a cylindrical microchannel [45][46]:

$$Q = \int_0^{2\pi} \int_0^a u(r)\phi r d\phi dr = \frac{-\pi a^4}{8\mu}\frac{dP}{dx} - \frac{\pi a^2 \varepsilon \zeta E}{\mu} f \tag{3.2}$$

In this equation, the function f takes into account the size effects of the electrical double layer and varies from zero to one. If the function tends to unity, that means that the velocity across the channel tends to be uniform and that the pore size is relatively larger than the Debye length. On the contrary, when the function f tends to zero, that means that there is a large overlap of the EDL and the velocity profile is therefore curved. The function f can be expressed as [46]:

$$f = \int_0^a \left(1 - \frac{\Psi}{\zeta}\right)\frac{2r}{a^2}dr = 1 - \frac{2I_1(a)}{aI_0(a)} \tag{3.3}$$

In this equation, I_0 and I_1 represents the modified Bessel functions of the first type of order zero and one, respectively, as represented in Figure 3.7a. The function f modeling the ratio between the radius of the channel and the Debye length is represented in Figure 3.7b.

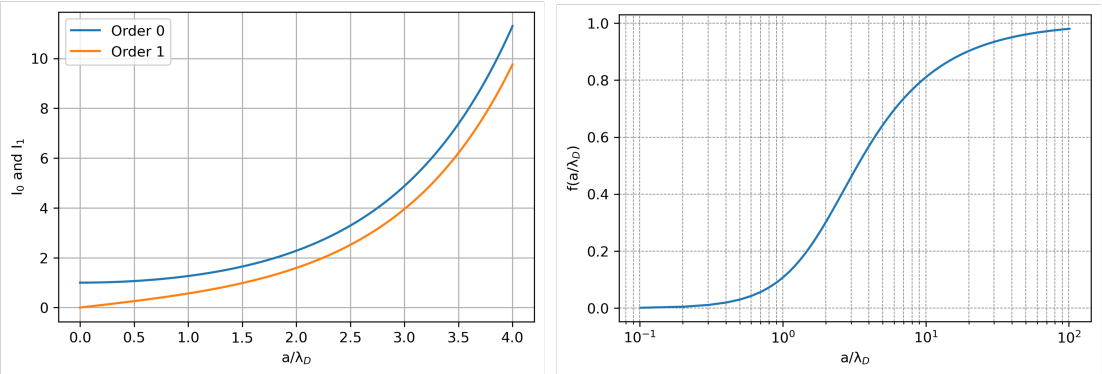

(a) (b)

Figure 3.7: (a) Modified Bessel functions of the first type of order zero and one. (b) Values taken by the function f in relation to the ratio between the channel radius and the Debye length.

For an array of cylindrical microchannels, the porosity and the tortuosity must be taken into account in the equation of the volume flow rate. Shuhuai Yao et al. determined this value, given in m^3/s in [25] [47] as:

$$Q = \frac{\psi}{\tau}\left[\frac{-a^2 A}{8\mu L}\Delta P - \frac{\varepsilon \zeta E A}{\mu} f\right] \tag{3.4}$$

In summary, parameters influencing the volume flow rate are the porosity ψ, the tortuosity τ, the geometry of the channel (with the cross-sectional area A, the radius a and the length L), the applied pressure ΔP, the zeta potential ζ, the axial electric field intensity E and the viscosity and permittivity of the fluid, respectively μ and ε.

The tortuosity is the capacity of the channel to be curved. It is defined as:

$$\tau = \left(\frac{L_e}{L}\right)^2 \tag{3.5}$$

with L_e and L, respectively the characteristic length of flow displacement along the channel path and the physical length of the channel. A tortuosity equal to one indicates that the channel is straight, with an easier flow displacement [48].

Porosity is defined as the ratio of the volume of pores V_p in a material to the volume of bulk V:

$$\psi = \frac{V_p}{V} \tag{3.6}$$

The more a material is porous, the more volume of fluid can pass trough it because the more charges are attracted to the substrate. Therefore, an electroosmotic pump is more efficient if the porosity of the substrate is high [48].

The maximum flow rate, Q_{max}, and maximum pressure, ΔP_{max}, of the pump can be derived from equation 3.4 as:

$$Q_{max} = \frac{-\psi}{\tau}\frac{\varepsilon\zeta AE}{\mu}f \tag{3.7}$$

$$\Delta P_{max} = \frac{-8\varepsilon\zeta V_{app}}{a^2}f \tag{3.8}$$

These equations show that, for a given value of the function f, flow performance is related to high electric fields and large cross-sectional areas, while maximum pressure is related to small pore diameters [48].

CHAPTER 4

NUMERICAL SIMULATIONS

In this chapter, a detailed analysis of the calculation methodology employed in Comsol Multiphysics is presented, outlining how this software is used to model and simulate the experimental system.

The Comsol Multiphysics software is used for the creation of physics-based models and simulation applications. In this particular study, the software is employed to simulate the electroosmotic phenomenon occurring as discussed in subsection 3.2.1. The primary objective of this numerical analysis is to determine the flow movement and flow rate achievable by pumping through the experimentally used membranes.

4.1 Flow velocity model

The solution to the flow equation for a nanopore described in chapter 3.2.5 (equation 3.2) is obtained by developing the Navier-Stokes equations describing fluid motion. These equations represent all the forces interacting with the fluid, including the forces of inertia. In microfluidics, these inertial forces are generally neglected due to the low Reynold's number of flows, which are then considered laminar.

The equation of Navier-Stokes for a laminar incompressible flow and the continuity equation are given by:

$$-\nabla p + \mu \nabla^2 \mathbf{u} + \mathbf{f} = 0 \tag{4.1}$$

$$\nabla \cdot \mathbf{u} = 0 \tag{4.2}$$

where $\mathbf{u}$ is the fluid velocity, p is the pressure, μ is the fluid viscosity and $\mathbf{f}$ represents the body force. In this case, the force $\mathbf{f}$ is the electroosmotic force acting on the charges in solution and is equal to:

$$f = \rho_e E_z = (F \sum_{i=1}^{N} z_i c_i) E_z \tag{4.3}$$

where E_z is the external electric field applied in the axial direction inside the nanopore and ρ_e represents the net charge density of species in solution [49]. This variable depends on the ion concentrations of the liquid. As the only electrolyte used in this work is water, the two ion species in solution are H_3O^+ and OH^-. A further assumption to be made is that there is a zero pressure gradient between the two ends of the pore. Therefore, the equation of Navier-Stokes describing the movement of the fluid inside the pore is written as:

$$\mu \nabla^2 \mathbf{u} + F(-c_{OH^-} + c_{H_3O^+}) E_z = 0 \tag{4.4}$$

where F denotes the Faraday constant, and c_{OH^-} and $c_{H_3O^+}$ are the ionic concentrations of the respective ions.

The transport of these ions inside the pore can be resolved by the equations of Nernst-Planck. It describes the molar flux of each ith species due to electromigration ($\mathbf{J}_i^e$), diffusion ($\mathbf{J}_i^D$) and convection. In steady state, the Nernst-Planck and the continuity equations are expressed as follows:

$$\mathbf{J}_i = \mathbf{J}_i^e + \mathbf{J}_i^D + \mathbf{u} c_i = -\frac{z_i F}{RT} D_i c_i \nabla \phi - D_i \nabla c_i + \mathbf{u} c_i \tag{4.5}$$

$$\nabla \cdot \mathbf{J}_i = 0 \tag{4.6}$$

In theses equations, D_i is the diffusion coefficient of the ionic species, z_i and c_i are the charge number and the concentration of each species, R is the gas constant, T is the absolute temperature and ϕ represents the electric potential.

The electric potential ϕ is given by the Poisson equation:

$$\nabla^2 \phi = -\frac{\rho_e}{\varepsilon} = -\frac{F(-c_{OH^-} + c_{H_3O^+})}{\varepsilon_0 \varepsilon_e} \tag{4.7}$$

where ε_0 and ε_e represents the permittivity of vacuum and the dielectric constant of the electrolyte.

4.2 Geometry of the problem

4.2.1 Boundary conditions

The geometry studied is a cylindrical pore of length L and radius R between two reservoirs of height H. Only half the system is modeled due to the symmetry of the problem, reducing the calculation dimension. Figure 4.1 illustrates the numerical domain in (a) and depicts certain imposed boundary conditions in (b) and (c).

The nanopore has a surface charge density of σ that is equal to the displacement electric field $\mathbf{D}$ multiplied by $\mathbf{n}$, the unit vector normal to the boundary surface. In the reservoirs, this displacement field is equal to zero. Moreover, the electric potential in each reservoir is equal to the external applied tension.

A pressure flow of zero, perpendicular to the pore cross-section, is imposed at the inlet and outlet of the pore using reservoirs filled with distilled water. The dissolved species in the solution are thus the products of water autoprotolysis, namely H_3O^+ and OH^- ions. The concentrations of these ions, denoted as c_i, are identical in each reservoir. On the other hand, there is no ion flux $\mathbf{J_i}$ at the surface of the pore. Moreover, a no-slip condition is enforced at the surface of the pore, resulting in a velocity vector $\mathbf{u}$ of zero at the pore walls.

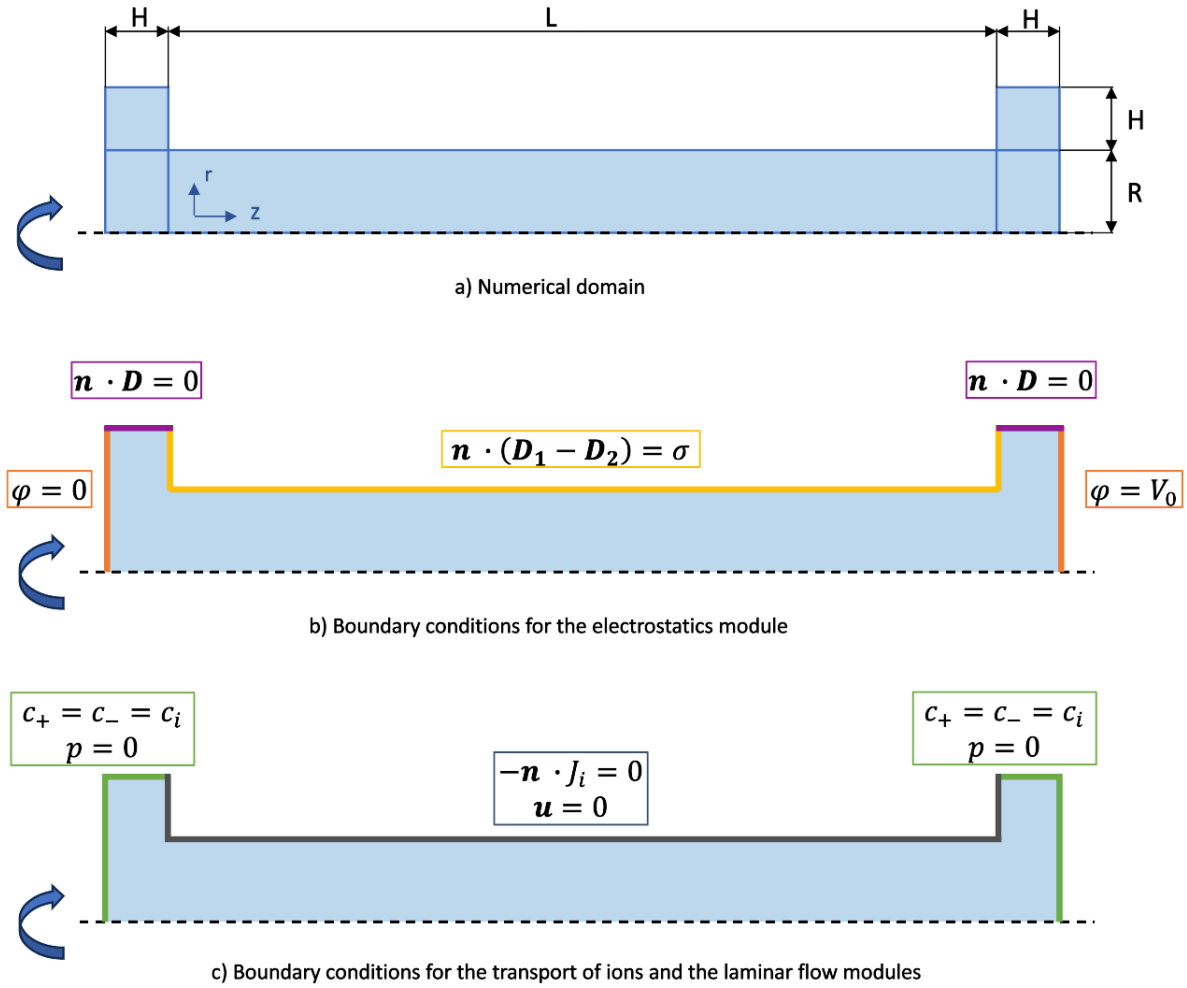

Figure 4.1: a) Numerical domain for a nanopore with reservoirs on either side. b-c) Boundary conditions for the same nanopore.

4.2.2 Numerical resolution

The method of finite elements is used to numerically resolve this problem. As it can be seen in Figure 4.2, a rectangular mesh is used.

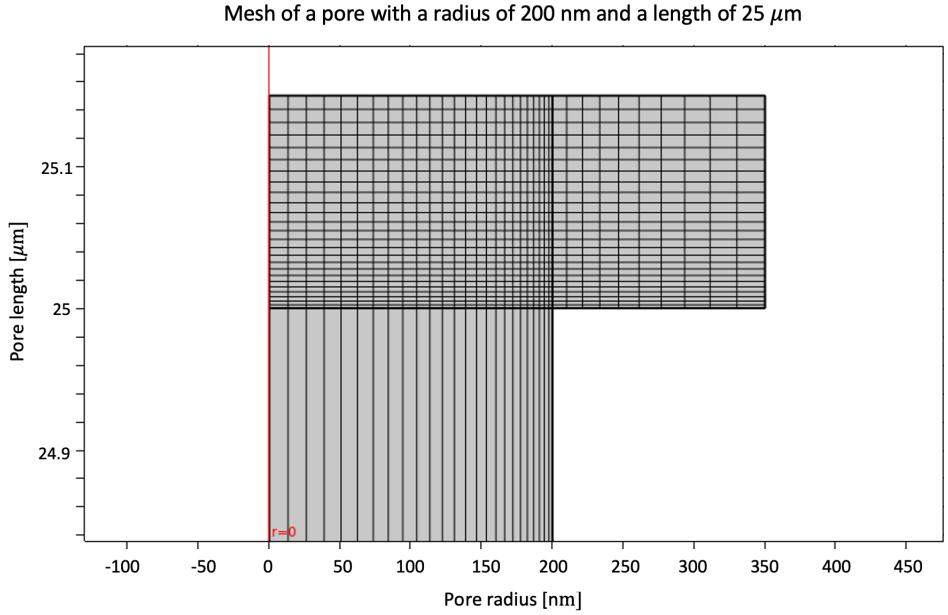

Figure 4.2: Mesh used for the numerical resolution with the finite element method. Only one reservoir and a part of the nanopore are shown.

For the pore surface, a fixed number of 60 elements is used. As variations in the electrical double layer increases exponentially towards the surface, more elements per surface unit are needed to capture these variations. Therefore, an element ratio is imposed radially, allowing the mesh elements to decrease as they approach the pore surface. Indeed, 25 elements are used to simulate the pore radially, with rectangles 4 times larger towards the center of the pore than towards its surface.

Some physical values are inserted in the software to numerically solve the problem. As mentioned before, the work electrolyte is distilled water. Therefore, the relative permittivity of the fluid is equal to 80.2 and its viscosity to 10^{-3} Pa s [50]. Moreover, the diffusion coefficient of ions OH^- and H_3O^+ are respectively $5.27 * 10^{-9}$ m^2/s and $9.31 * 10^{-9}$ m^2/s [51]. As pH of DI water is approximately 5 when exposed to air, the concentrations of ions is defined at 10^{-3} mol/m^3 [52]. Using equation 2.1, the Debye length is approximately 100 nm at room temperature.

Moreover, experiments are performed with an applied tension of 100 V. Knowing the distance of 2.4 cm between both electrodes allow us to calculate the electric field in the EOP ($E = U/d$). Based on this value, the tension that has to be applied in the numerical simulation for a membrane thickness of 25 μm is 104.16 mV, in order to be as close a possible to the experiments.

The determination of surface charge density in the numerical simulation is also an important parameter. In accordance with equation 2.4 $\zeta = \frac{\sigma\lambda_D}{\varepsilon}$ presented in chapter 2.1.3, surface charge density, denoted as σ, is directly proportional to the zeta potential, symbolized as ζ. This value can vary significantly depending on the specific measurement conditions. Factors such as the concentration of ions in the electrolyte, the pH of the solution, and the material itself contribute to this variability. To provide some insight into the range of zeta potential values for different materials, several articles have reported relevant information. For PC for example, studies [53] and [54] indicate a range of -18 to -28 mV when distilled water is used as the working electrolyte. Another study [55] suggests values ranging from -10 to -40 mV, depending on the pH of the solution. Zeta potentials found in literature for each material used in this study are provided in table 4.1. To be able to fix a particular value for each material, article [56] gives a classification of zeta potentials for polymers in the same conditions, determining that $\zeta_{PI} > \zeta_{PC} > \zeta_{PE}$. Finally, based on equation 2.4, surface charge density is determined for each material.

Table 4.1: Range of zeta potentials of various materials according to the literature, selected value to be implemented in the simulation and corresponding surface charge density.

Material	References	Range of zeta potential [mV]	Zeta potential [mV]	Surface charge density [C/m^2]
PC	[53][54][55]	[-10, -40]	-25	-1.75 $*10^{-4}$
PE	[55]	[0, -25]	-15	-1.035 $*10^{-4}$
PI	[57]	[-30, -60]	-40	-2.76 $*10^{-4}$
Al_2O_3	[58][59]	[40, 50]	45	3.105 $*10^{-4}$
PSi	[60][61]	[-8, 20]	-14	-9.66 $*10^{-5}$

4.3 Results

As described in equation 3.4, electroosmotic velocity in a nanopore depends on various parameters. In this section is explained how some of these parameters, i.e. the zeta potential ζ, the pore size a and the thickness L, influences the velocity magnitude at the center of the pore. The basic configuration for numerical simulations is done for a polycarbonate half-pore with radius of 200 nm, thickness of 25 μm, applied tension of 104 mV and with deionized water as the working electrolyte.

As shown in Figure 4.3a, the amplitude of the electroosmotic velocity varies with the zeta potential of the pore surface as it is strictly proportional to the ζ

of the material. It can also be seen from Figure 4.3b that the velocity magnitude changes sign with opposite zeta potential. This means that the velocity of an alumina membrane, with $\zeta = 45$ mV is negative while that of a polycarbonate membrane, with $\zeta = -25$ mV, is positive.

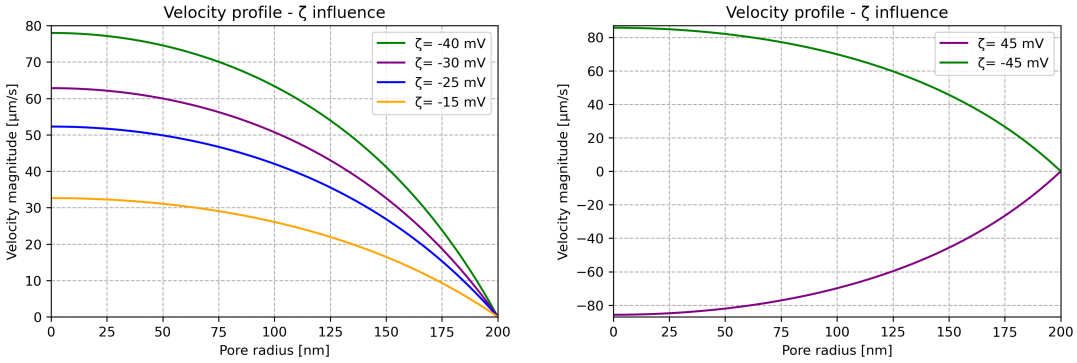

(a) (b)

Figure 4.3: Influence of zeta potential on pore cross-section velocity profile.

Figure 4.4 shows the variation of velocity magnitude depending on the pore size. One can see that the profile varies with pore size in two ways. In large nanopores, i.e. when the ratio between the pore radius and the Debye length is relatively larger than 1, the velocity profile appears to be flat. Moreover, the electroosmotic velocity magnitude is constant for large channels and does not depends on the pore radius. This behavior is evident when comparing pore radii of 600 nm and 1.5 μm, where both exhibit the same maximum electroosmotic velocity. At the opposite, when the ratio between the pore radius and the Debye length becomes smaller than 1 (for a < 0.1 μm), there is a recovery of the electrical double layer in the nanopore. This induces a curved velocity profile. Moreover, the maximum electroosmotic velocity within nanochannels decreases with decreasing channel size.

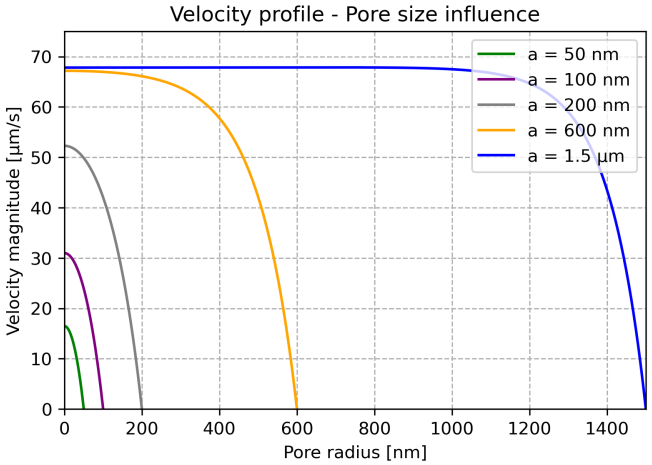

Figure 4.4: Influence of the pore size on pore cross-section velocity profile.

The pore length L also influences the velocity profile. As it can be seen in Figure 4.5, the velocity magnitude is proportional to the membrane thickness and decreases with it.

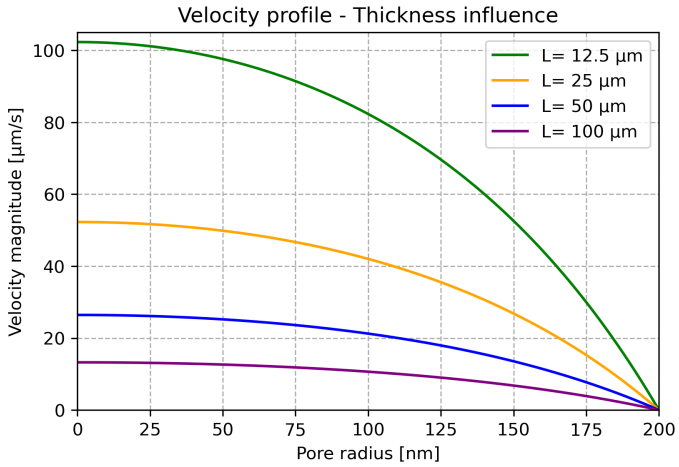

Figure 4.5: Influence of membrane thickness on pore cross-section velocity profile.

The charge distribution in the nanopore can be determined numerically. As observed in Figure 4.6, the concentration of H_3O^+ ions is highest at the pore surface and decreases as it reaches the center of the pore. This decrease corresponds to the electric double layer, as explained in chapter 2.1.2. Furthermore, since the pore radius is 200 nm, the thickness of the region of high ion concentration (between

20 and 35 mmol/m^3) is around 100 nm. This confirms that the Debye length is of 100 nm.

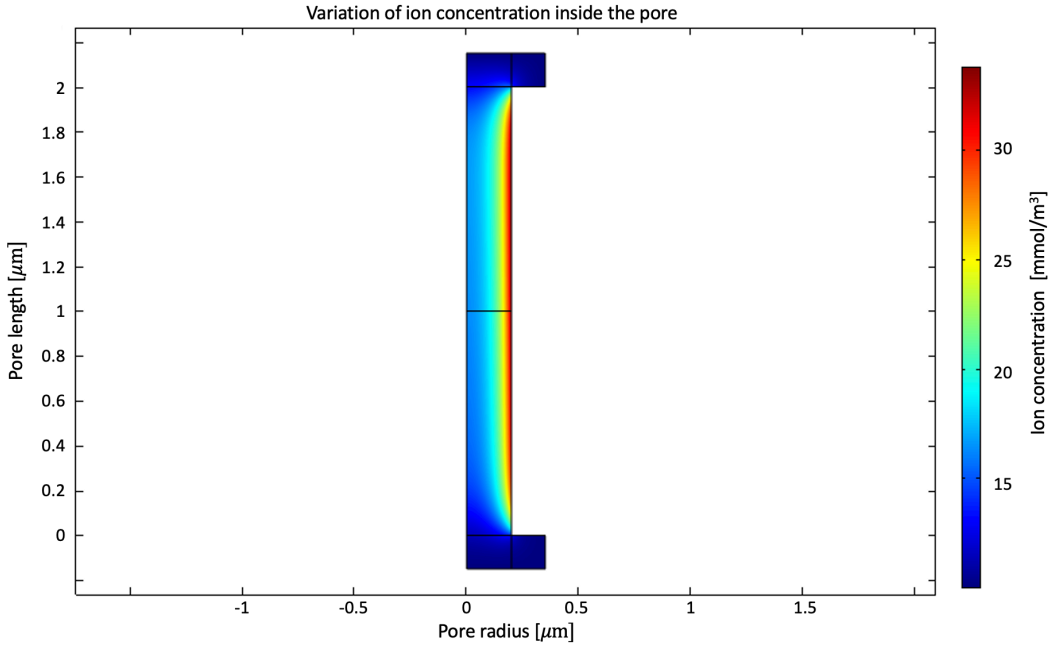

Figure 4.6: Variation in the concentration of H_3O^+ ions in a nanopore with a radius of 200 nm and a length of 2 μm.

CHAPTER 5

RESULTS

This chapter begins by a characterization of the various membranes used for this work. It subsequently provides a summary of the flow rate outcomes corresponding to each membrane. Finally, a comparison among the experimental, analytical, and numerical results is presented.

5.1 Membranes characterization

To be certain of the various characteristics of the membranes used for the electroosmotic pumping, some analyses are made. The membranes are firstly characterized by the scanning electron microscope (SEM). The images captured by the SEM are then analyzed by the software ImageJ. The hereunder characterized membranes are the ones with a pore size of 100 nm according to the manufacturer, with and without surface modifications.

5.1.1 Membrane without any surface modification

The first characterized membrane is in polycarbonate (PC) and has a pore size of 100 nm according to the manufacturer. This membrane is shown in Figure 5.1a.

Analyzing the image taken by the SEM with ImageJ software, the pore size does not appear to be of 100 nm. By taking the average diameter of the pores on this image, the mean pore size appears to be of 152 nm. However, some pores are not taken into account because they are merged with each other. Indeed, these pores

are no longer circles and the average diameter is distorted. This is shown in Figure 5.1b.

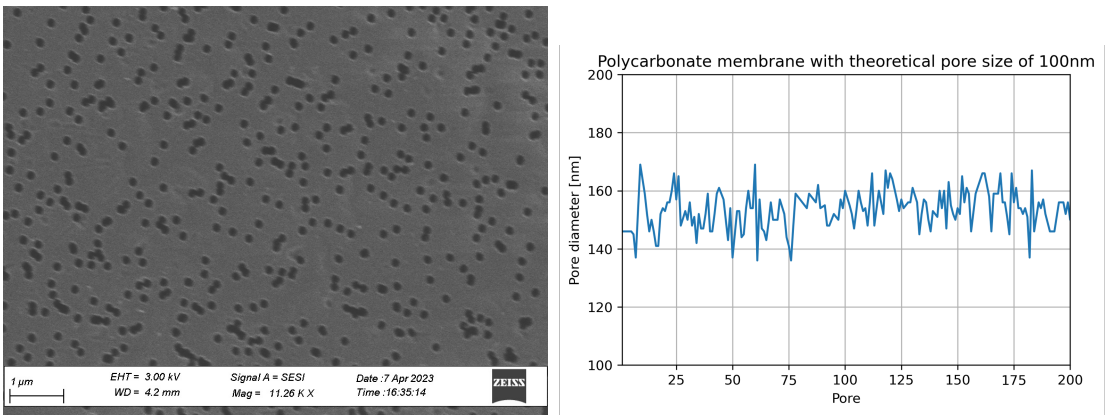

(a) (b)

Figure 5.1: (a) SEM image of a PC membrane with theoretical pore size of 100 nm. (b) Diameter of all pores not merged in the image taken by the SEM.

A second parameter that differs from the manufacturer's announcement is the membrane porosity. The suggested porosity of this membrane is 4.7%. By analyzing various images of this membrane, it appears that the real porosity of it is 12.9%, which is more than double the value initially announced.

5.1.2 Membrane with atomic layer deposition

The first treated membrane is in polycarbonate and was subjected to 50 ALD cycles of Al_2O_3. SEM images confirm successful deposition. Before surface treatment, the pore size was 152 nm. After 50 ALD cycles, the average pore diameter of the membrane is 140.5 nm. Zijing X. et al. achieved a similar deposition in [62]. By performing 100 ALD cycles on alumina, the thickness of the deposit was of 12.2 nm. Therefore, when performing 50 ALD cycles, the thickness should be 6.1 nm. In view of the decrease in pore size observed in the SEM, the deposit thickness is 5.75 nm in this work, which is close to the value reported by Zijing X. et al.

A second alumina deposit was applied on the same membrane. The aim of this deposition is to considerably reduce the pore size of the membrane. To achieve this, alumina deposition applied to the polycarbonate membrane was carried out over 200 ALD cycles. The membrane was analyzed by SEM after deposition, as shown in Figure 5.2.

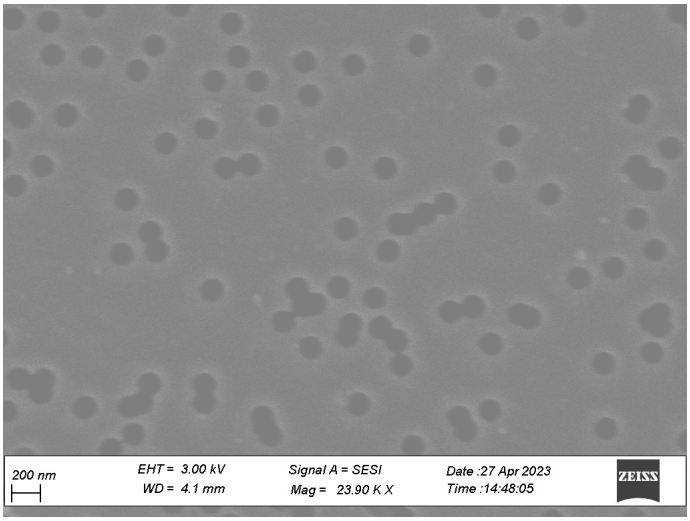

Figure 5.2: SEM images of a membrane in PC with pore size of 152 nm that has undergone 200 ALD cycles of Al_2O_3.

In the same way as for the membrane without surface modification, pore size is analyzed. Atomic layer deposition succeeded to reduce pore size. However, a 48.8 nm reduction in pore diameter is expected. By analyzing SEM images, the pore size of the membrane that has undergone 200 ALD cycles averages 136.6 nm. This results in a reduction in pore diameter of around 15 nm, which is not the expected result.

A similar phenomenon has been observed by Fengbin L. et al. in [63]. They observed that ALD reduces pore size non-linearly with the number of cycles. The rate of reduction is high during the period from 0 to 200 ALD cycles of alumina, with a maximum pore size of 50 nm, but slows down during the period up to 600 cycles, when the pore size becomes smaller than 50 nm. The explanation for this non-linear reduction may lie in the involvement of the TMA precursor in the deposition. Indeed, the smaller the pore size, the more the diffusion of the precursor into the pores is limited by their size. As a result, the rate of alumina deposition is reduced as pore size decreases. Despite the different characteristics of their study compared to this one, this explanation could be a lead to follow to understand the small reduction in pore size with 200 ALD cycles.

5.1.3 Membrane with gold deposition

As explained in section 3.1.2, a gold metallization of one side of some membranes was performed. This surface modification can be observed in Figure 5.3. This SEM

image proves that the gold has been well deposit on the surface as the surface morphology has changed and gold nanoparticles can be observed all over it.

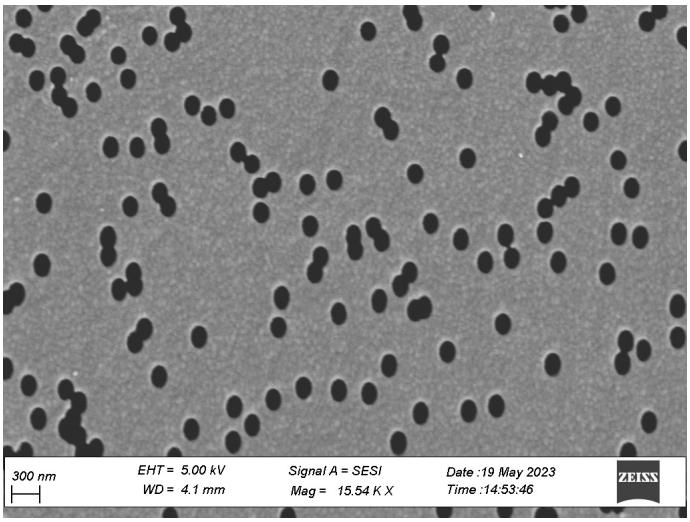

Figure 5.3: SEM images of a membrane in PC with pore size of 152 nm coated with gold.

The average pore size observed in this membrane is 168.55 nm. The pore size of this membrane without the gold coating was of 152 nm. This metal deposition therefore has the effect of increasing the pore size by approximately 16 nm.

A number of hypotheses have been put forward to explain this phenomenon of increased pore size. Firstly, a thermal degradation of the membrane during the process was imagined. After some research, this hypothesis was dismissed because of the parameter used in the metallization device. The device does not normally exceed 110°C. Moreover, no thermal degradation has ever been observed for photoresins, which degrade above 150°C. As the glass transition temperature of PC is 140°C, thermal degradation of the membrane would be unexpected.

Moreover, as the pores seen in image 5.3 are still uniform, any degradation is also neglected as it would degrade the membrane non-uniformly. Consequently, a hypothesis on the parameters affecting the SEM image scale is put forward. Since a polycarbonate membrane is non-conductive, charges build up in the material as electrons from the incident beam are trapped there. In a conductive material, i.e. in this gold-coated membrane, this charge effect does not occur. This effect can lead to the need to modify certain SEM parameters. For example, brightness or contrast have to be adjusted, and these parameters are taken into account in the

ImageJ software to determine pore size. The impact of this material difference in the SEM could be a lead to follow to explain the increase in pore size with metallization.

5.1.4 Summary

Table 5.1 is a summary of the membranes studied for this work. They vary by the material used, the geometry and the surface treatments applied on it.

Table 5.1: Table of the various membranes used for electroosmotic pumping during this work.

N°	**Material**	**Pore size [nm]**	**Porosity [%]**	**Thickness [μ m]**	**Surface modification**
1	PC	3000	21.2	22	None
2	PET	3000	21.2	20	None
3	PC	1200	17.3	24	None
4	PC	400	18.8	25	None
5	PET	400	18.8	23	None
6	PI	400	18.8	25	None
7	PC	233	15.7	25	None
8	Al_2O_3	200	37	60	None
9	PC	152	12.9	47	None
10	PSi	25	39.9	100	None
11	PC	250	16.8	47.05	Metallization
12	PC	168	14.25	47.05	Metallization
13	PC	140.5	11.88	25	50 ALD cycles
14	PC	136.6	11.59	25	200 ALD cycles

5.2 Experimental results

5.2.1 Variation of material and pore size

The first experimental results in terms of flow performance are obtained for membranes of varying pore size and material, without surface modifications. Two types of results are obtained: regular flow and non-regular flow, with the appearance of a transient regime before reaching a permanent flow regiment.

A methodology is defined to be able to compare flow results with all membranes. If the flow produced by the pump is stationary, the flow value derived from it is

constant. On the other hand, if the flow is not stationary, a time must be defined at which the flow measurement is no longer irregular. The flow rate obtained by electroosmotic pumping for membrane 1 over time is shown in Figure 5.4. It shows 3 different experiments produced under the same experimental conditions. We can deduce from this graph that after 20 minutes of pumping, the flow rate becomes regular. The comparative flow value for any membrane without surface modifications and undergoing a transient regime is therefore determined from 25 minutes of pumping.

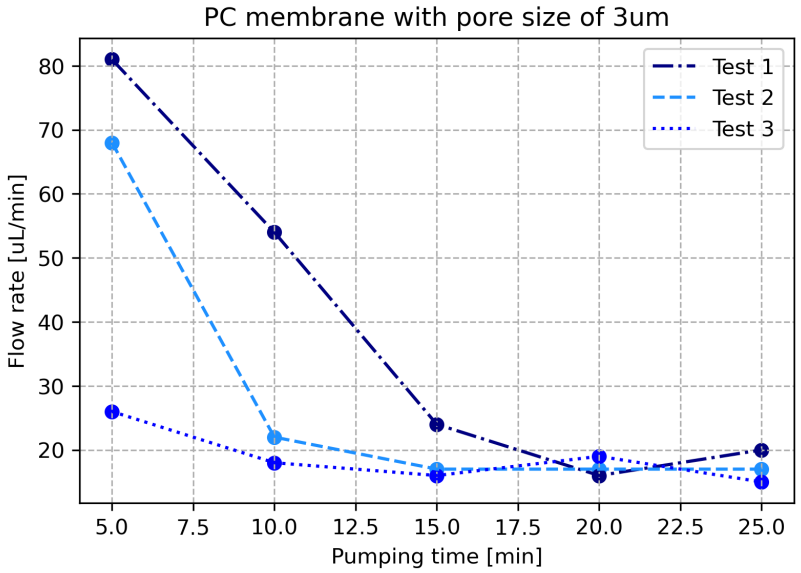

Figure 5.4: Flow rate in absolute value obtained for 3 various experiments carried out in the same conditions, with a transient and a steady state. Experimental conditions are the ones explained in chapter 3.2.1.

Figure 5.5 shows the various flow rates obtained experimentally using the electroosmotic pump for membranes 1 to 9 in table 5.1. The maximum flow rate achieved is -17 μL/min and is obtained for the polycarbonate membrane with a pore diameter of 3 μm. For a fixed pore size of 0.4 μm, polyimide shows the best performance in terms of flow compared with polyethylene and polycarbonate.

Another result worth highlighting is the flow rate of 9 μL/min obtained for the pump using an alumina membrane with a pore size of 200 nm (membrane 8 in table 5.1). The flow is of the opposite sign to those observed with the previous membranes. Moreover, with the same pore diameter, the PC membrane exhibits a relatively smaller flow rate in absolute value, of -3 μL/min.

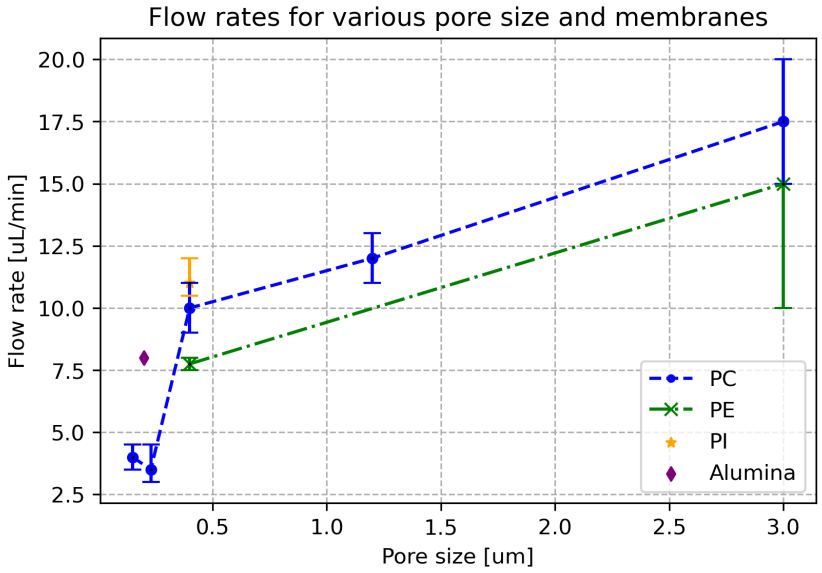

Figure 5.5: Flow rate in absolute value obtained for 4 various materials (PC, PE, PI and Al_2O_3) and varying pore size (from 0.2 μm to 3 μm). Vertical bars represents the confidence interval.

The last material tested in this work is porous silicon. The PSi membrane used has a pore size of 25 nm and is 100 μm thick. Using this membrane, no flow was observed after 24 hours of pumping.

5.2.2 Metallization

Two PC membranes were subjected to a gold deposition, with pore sizes of 168.55 nm and 250.10 nm (membranes 11 and 12 respectively in table 5.1). The flow rate obtained for these two membranes is compared in Figure 5.6 with the one of the initial PC membranes without surface modification.

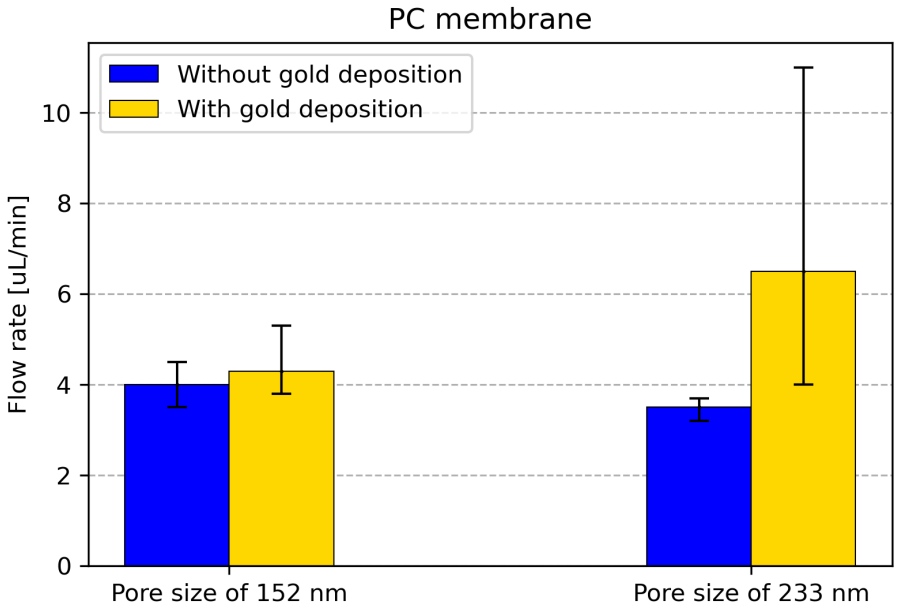

Figure 5.6: Comparison of experimental flow rates in absolute values obtained for membranes with and without metallization. Flow rates are determined after 30 minutes of pumping for all membranes. Vertical bars represents the confidence interval.

The maximum flow rate obtained is -6.5 μL/min and concerns the membrane with an initial pore size of 233 nm which has undergone metallization. The membrane delivers a flow rate 1.85 times greater than the same membrane without deposition. The increase in flow rate between membranes with and without metallization, and with an initial pore size of 152 nm is less significant with a flow rate 1.12 times higher.

5.2.3 Alumina deposition

Two ALD of Al_2O_3 were deposited on a polycarbonate membrane with a pore size of 152 nm (membranes 13 and 14 in table 5.1). Deposits were of 50 and 200 cycles. Figure 5.7 shows the different flow rates obtained with these membranes.

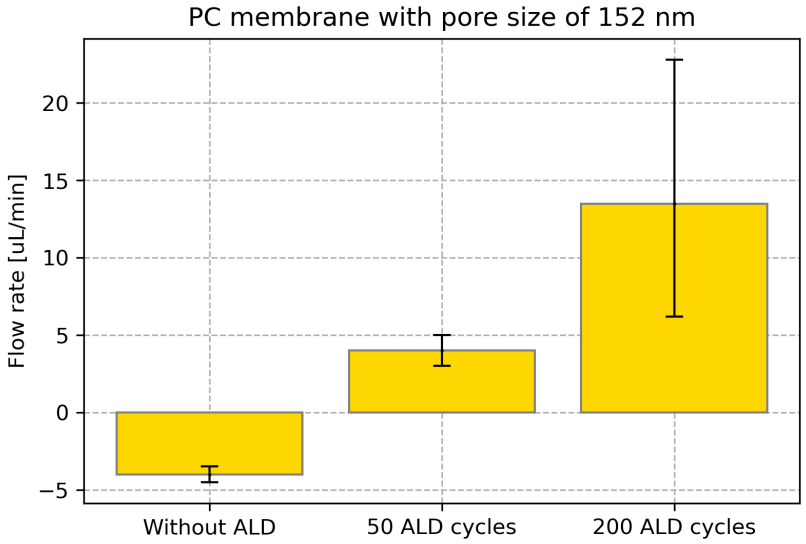

Figure 5.7: Comparison of experimental flow rates obtained with the same initial membrane in 3 various conditions: without surface modification, with 50 ALD cycles of Al_2O_3 and with an 200 ALD cycles of the same material. Flow rates are determined after 40 minutes of pumping. Vertical bars represent the confidence interval.

The experimental flow rates for both membrane with alumina deposition are positive, in contrast to the membranes without surface modification. The maximum flow rate in absolute value is observed for the membrane with 200 ALD cycles and is 13.5 μL/min. Furthermore, experiments with membranes with 50 ALD cycles of alumina show a transient regime that stabilizes after 35 minutes of pumping.

5.3 Comparison of experimental, numerical and analytical results

As mentioned in section 5.2, experimental results demonstrating the performance of the pump's electroosmotic flow rate have been obtained. These results can be compared with two other flow rate resolutions: analytical and numerical. Analytical flow rates are obtained using equation 3.2, determining the volume flow rate for a cylindrical microchannel:

$$Q = \frac{-a^2 A}{8\mu L}\Delta P - \frac{\varepsilon\zeta E A}{\mu} f \tag{5.1}$$

This value must be multiplied by the number of pores in each membrane, to determine the analytical flow rate value as close as possible to the experimental conditions. In equation 5.1, the parameter f plays a crucial role in interpreting the overlap of the double layer as pore size decreases. This parameter is found for all membranes in the table below. The software Comsol Multiphysics has been used to numerically find the solution to the flow rate equation in the electroosmotic pump. This numerical resolution is based on the development explained in chapter 4.1.

Table 5.2 summarizes the main characteristics of the membranes used experimentally in this work. It also shows the flow rates obtained in three different ways for each membrane: experimentally, analytically and numerically. Three boxes in this table are empty. This is because, as mentioned above, no flow could be observed experimentally for porous silicon. In addition, the value of the zeta potential must be known in order to determine the analytical flow as well as the numerical flow. As mentioned in article [62], the addition of an alumina layer by atomic layer deposition increases the zeta potential of the substrate used in their study. Unfortunately, no papers could be found estimating the increase in ζ by the addition of 50 or 200 ALD cycles on a polycarbonate membrane. Consequently, numerical and analytical resolution of the flow rate for a PC membrane with ALD could not be achieved.

Table 5.2: Various characteristics of each membrane used in this work and determination of the flow rate pumped by each membrane in three ways: experimental, analytical and numerical. The value of the experimental flow rate is the mean value obtained for a minimum of 3 experiments. The variance of each experimental value is detailed in section 5.2.

N°	**Material**	**Pore size [nm]**	**Porosity [%]**	**Thickness [μm]**	**f**	**Experimental flow rate [μL/min]**	**Analytical flow rate [μL/min]**	**Numerical flow rate [μL/min]**
1	PC	3000	21.2	22	0.93	-17.5	-24.98	-49.11
2	PE	3000	21.2	20	0.93	-15	-14.98	-33.07
3	PC	1200	17.3	24	0.84	-12	-18.83	-32.43
4	PC	400	18.8	25	0.57	-10	-13.96	-18.55
5	PE	400	18.8	23	0.57	-7.75	-8.38	-12.42
6	PI	400	18.8	25	0.57	-11	-22.34	-28.16
7	PC	233	15.7	25	0.36	-3.5	-6.63	-10.48
8	Al_2O_3	200	25-50	65	0.30	9	15.25	15.58
9	PC	152	12.9	47	0.21	-4	-2.72	-5.83
10	PSi	25	39.1	100	0.0077	/	-0.28	$-6.24 * 10^{-3}$
11	PC + gold	250	16.8	47.05	0.39	-6.5	-15.06	-23.94
12	PC + gold	168	14.25	47.05	0.24	-4.3	-6.21	-14.15
13	PC + 50 ALD cycles	140	11.88	25	0.19	4	/	/
14	PC + 200 ALD cycles	136	11.59	25	0.18	13.5	/	/

Figure 5.8 gives a better idea of the relationship between the three types of results. It shows the flow rate as a function of pore size for a polycarbonate membrane (membranes 1-3-4-7), for experimental, analytical and numerical resolution. All results show the same tendency, as flow rate increases with pore size. Moreover, the best flow rate for all pore size is obtained with numerical resolution, and analytical resolution gives also a better flow performance than the experiments.

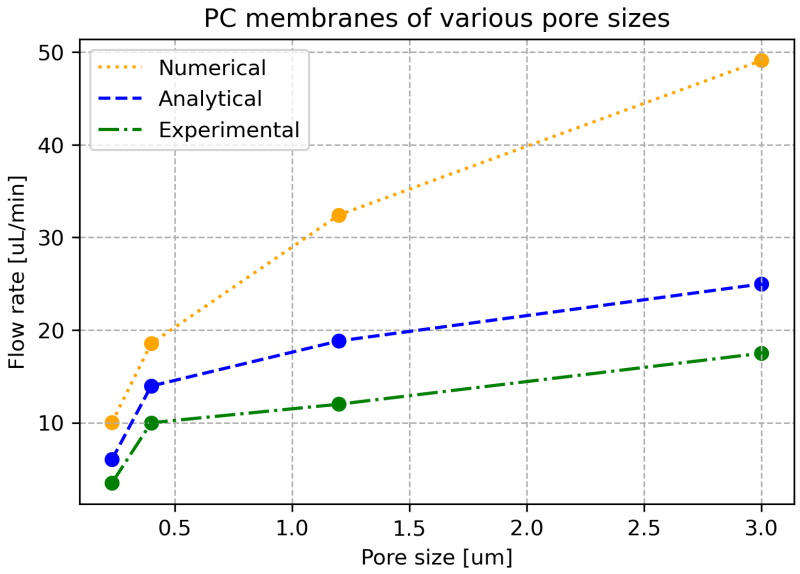

Figure 5.8: Volume flow rate in absolute value obtained for a polycarbonate membrane with pore size varying from 0.2 μm to 3 μm. Three resolutions of the pump flow performance are shown: numerical, analytical and experimental.

CHAPTER 6

DISCUSSION

This chapter aims to discuss the results obtained in the previous section. It analyzes how membrane characteristics (pore size and material) influence the experimentally observed flow rate. It establishes the correlation with the zeta potential and surface charge density of each membrane. The impacts of surface modifications on the flow rate are also examined. Finally, a hypothesis to explain the differences between experimental, analytical, and numerical results is provided.

6.1 Influence of membrane characteristics on flow performance

6.1.1 Influence of material

Polymers and alumina

Experimental results obtained with different polymers show that, for a membrane with identical characteristics, polyimide offers the best flow performance, followed by polycarbonate and then polyethylene. In fact, PI demonstrates a flow rate 10% higher than PC and 42% higher than PE. This was determined on the basis of membranes with a pore size of 400 nm, identical porosity and almost identical thickness. Consequently, the only parameter that really influences flow and varies with material is zeta potential. This demonstrates that under the same experimental conditions, $\zeta_{PI} > \zeta_{PC} > \zeta_{PE}$. The literature confirms this ranking in article [56].

Furthermore, when comparing two membranes with virtually the same pore size, one made from 233 nm PC and the other from 200 nm alumina, Al_2O_3 shows 157% better flow performance than PC, despite a slightly smaller pore size and a thickness nearly twice larger. Moreover, the alumina membrane has a flow rate value opposite to the one of the polymers. Consequently, the zeta potential of alumina is higher in absolute value and of opposite sign than that of PC. In view of the ratio of 1.10 between the experimental flow rate of PI and PC versus that of 2.57 between alumina and PC, the hypothesis that $\zeta_{Al_2O_3} > \zeta_{PI}$ under the same experimental conditions can be made.

Based on the experiments carried out, zeta potentials could be obtained for each membrane discussed before using the equation 3.4 describing the flow in a cylindrical microchannel. These values are shown in table 6.1, together with the corresponding surface charge density values, determined from equation 2.4 linking these two parameters. This table confirms the hypothesis put forward earlier: $\zeta_{Al_2O_3} > \zeta_{PI} > \zeta_{PC} > \zeta_{PE}$ in absolute value for the same experimental conditions. As surface charge density is directly proportional to zeta potential, this ranking also applies to it. Alumina is therefore the most efficient material tested for use in an electroosmotic pump.

Table 6.1: Zeta potentials and surface charge density of membranes with various materials but virtually same other characteristics.

N°	**Material**	**Pore size** [**nm**]	**Experimental flow rate** [μ**L/min**]	**Zeta potential** [**mV**]	**Surface charge density** [**C/m^2**]
4	PC	400	-10	-18.21	-1.26E-4
5	PE	400	-7.75	-14.12	-9.74E-5
6	PI	400	-11	-20.03	-1.38E-4
7	PC	233	-3.5	-12.08	-8.34E-5
8	Al_2O_3	200	9	16.73	1.15E-4

Porous silicon

The porous silicon membrane can not be compared with any of the other membranes due to its different geometrical characteristics. It has a pore size of just 25 nm and a thickness of 100 μm. These characteristics considerably reduce the flow rate of this membrane. Compared with a membrane with a pore size of 400 nm and a thickness of 25 μm, flow rate would be 1024 times lower by considering only these two elements. Moreover, by considerably reducing the membrane's pore size, the overlap of the electrical double layer becomes more important. Since the

Debye length is considered to be 100 nm in deionized water, the ratio of pore radius to EDL is one-quarter, indicating that the overlap is very high. This would also considerably reduce flow rate, as the diffuse layer is significantly diminished. Furthermore, as reported in the literature, the zeta potential of porous silicon is between -8 and -20 mV, which is relatively lower than the zeta potentials of the other materials tested in this work. All these factors could possibly explain why no flow was observed experimentally for PSi after 24 hours of pumping.

In addition, numerical simulations show that a flow rate of $6.24 * 10^{-3} \mu$L/min is obtained for this PSi membrane. Therefore, over the course of a 24-hour experiment, a flow rate of approximately 9 μL should have been observed. However, the ratio between numerical and experimental flow rates for pumps with other membranes is between 1.45 and 3.27. Consequently, the experimental flow rate should be between 2.75 and 6.2 μL/day.

Furthermore, as SEM images have shown, porous silicon is not smooth inside the pores. As mentioned in [16], the EOF pumping effect decreases as the pore wall becomes rougher. However, this parameter is not taken into account in the numerical simulations. The fact that the inner pore wall is rough could therefore also explain why no flow was observed in the laboratory.

The final research question of this work concerns the determination of the surface charge density of a porous silicon membrane by experimentally determining the flow rate obtained by electroosmotic pumping. As no flow rate could be observed experimentally with this membrane, it is not possible to answer the question. Nevertheless, other materials as polymers and alumina were studied and surface modifications were carried out on some membranes. Surface charge density was therefore determined for theses polymer membranes.

6.1.2 Influence of pore size

Pore size has a considerable impact on electroosmotic velocity. As shown in Figure 5.5, flow increases with pore size. Actually, experimental flow rate increases by 150% as pore size increases from 150 to 400 nm, and by 20% as pore size increases from 400 to 1200 nm. As a matter of fact, as the numerical simulations show, the increase in electroosmotic velocity as a function of pore size is not linear. It reaches a level at a certain size and then stops increasing.

Based on equation 3.4, zeta potentials could be determined analytically from the flow rates obtained experimentally for each membrane. As shown in Figure

6.1, the zeta potential increases rapidly for smaller pore sizes and reaches a plateau for larger pores. This trend is similar to that of flow rate as a function of pore size. Furthermore, as surface charge density is proportional to zeta potential, its magnitude decreases as pore size increases. As mentioned in article [29] and in chapter 2.3.1, this phenomenon could be due to pore curvature. Indeed, as shown in Figure 6.1, as pore size decreases, curvature increases. As a result, fewer ionic groups are able to bind to the polymer surface. The more the curvature of the pore becomes flat, the more ions groups are able to bind the surface and interacts between themselves.

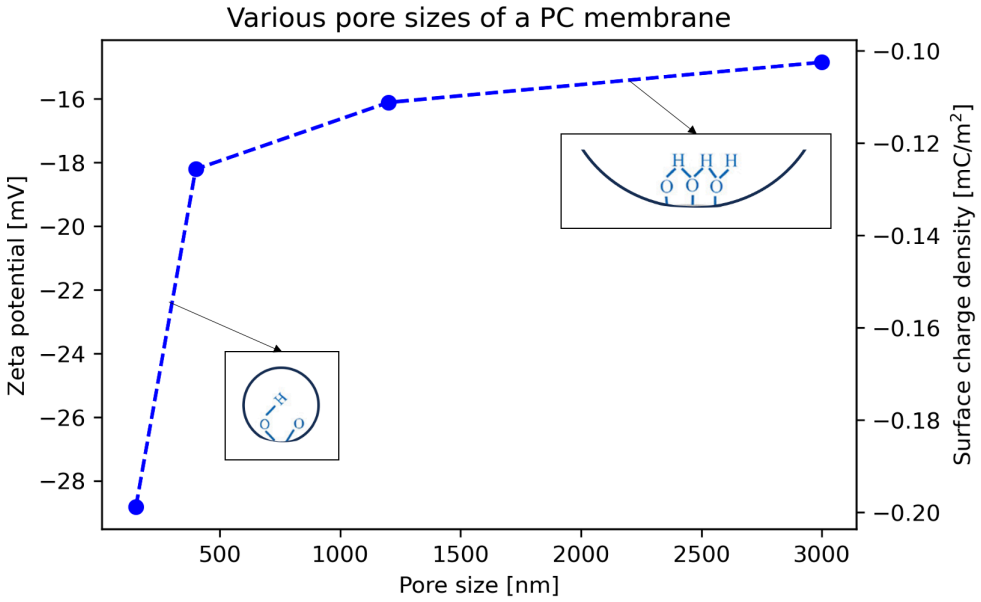

Figure 6.1: Zeta potentials and corresponding surface charge density for different pore sizes of a polycarbonate membrane. The curvature of the pore influencing both parameters is shown.

The determination of zeta potential as a function of pore size highlights another point. The zeta potential of the 233 nm diameter PC membrane is -12 mV [1]. It is therefore higher than those for the 150 nm and 400 nm membranes, which are -29 mV and -18 mV respectively. For this reason, the experimental results for the PC membrane with a pore size of 233 nm is not consistent with the results for the other membranes. Consequently, the flow rate obtained for this PC membrane is considered an outlier and is not taken into account in the discussion of other factors influencing surface charge density.

[1]This value has not been added to Figure 6.1 for the reason explained immediately below.

6.2 Influence of metallization on flow performance

From an analytical and numerical point of view, a metal deposition should result in a doubling of flow rate in an EOP. The metallized side of the membrane is thus considered as one of the two electrodes, halving the distance between them. As a result, the induced electric field is doubled and so is the flow rate obtained, as explained in chapter 3.2.5.

Experimental results show an increase in flow rate for both membranes subjected to metallization. The membrane with a pore size of 152 nm saw its flow rate increase by a factor of 1.12 with metallization, and the one with a pore size of 233 nm saw its flow rate increase by a factor of 1.85. In consequence, metallization of the membrane with pore size of 233 nm resulted in the expected flow rate increase. However, the membrane with a pore size of 152 nm did not show the same level of flow rate improvement.

6.3 Influence of ALD on flow performance

6.3.1 Determination of surface charge density

Experimental results show a reversal of flow direction with both membranes subjected to alumina surface deposition. This phenomenon is due to the opposite sign of the alumina zeta potential compared to the one of polymers. As mentioned in [58][59], ζ of PC is negative, whereas ζ of alumina is positive. By analytically determining the zeta potentials as a function of the experimental flow rates, table 6.2 shows the various results, together with the values of the surface charge densities.

Table 6.2: Summary of zeta potentials and corresponding surface charge densities of membranes subject to alumina deposition.

Membrane	**Experimental flow rate [μL/min]**	**Zeta potential [mV]**	**Surface charge density [mC/m^2]**
PC 152 nm	-4	-28.82	-0.20
PC 152 nm + 50 ALD cycles	4	34.6	0.24
PC 152 nm + 200 ALD cycles	13	121.6	0.84

As shown in the table above, the ζ of the PC membrane with 50 ALD cycles is higher than the one of the same membrane without surface modifications. In addition, this membrane shows an 8.5% reduction in pore size due to alumina deposition, which should decrease the ζ, as explained in section 6.1.2. This means that Al_2O_3 ALD significantly improves the performance of the polycarbonate membrane. Moreover, Zijing X. et al demonstrates in [62] that ALD of alumina significantly increases zeta potential of a SiO_2 membrane. In a solution with 0.01 M KCl, the native silica membrane has a ζ of approximately -10 mV. After 100 ALD cycles of alumina, the same membrane has a ζ of approximately 70 mV, which confirms the increase of ζ with ALD of alumina.

6.3.2 Membrane phenomenon after electroosmotic pumping

A SEM image of this membrane with 200 ALD cycles after using it in the electroosmotic pump has been taken and is shown in Figure 6.2. An intriguing phenomenon can be observed. In part 1 of the image, the pores are present and nothing in particular is observed. In part 2, on the other hand, the pores become clogged and disappear as we approach part 3. A uniform layer is formed. In part 3, a sort of crust has formed beyond the polycarbonate membrane. Moreover, where this crust is cracked, the pores are visible underneath.

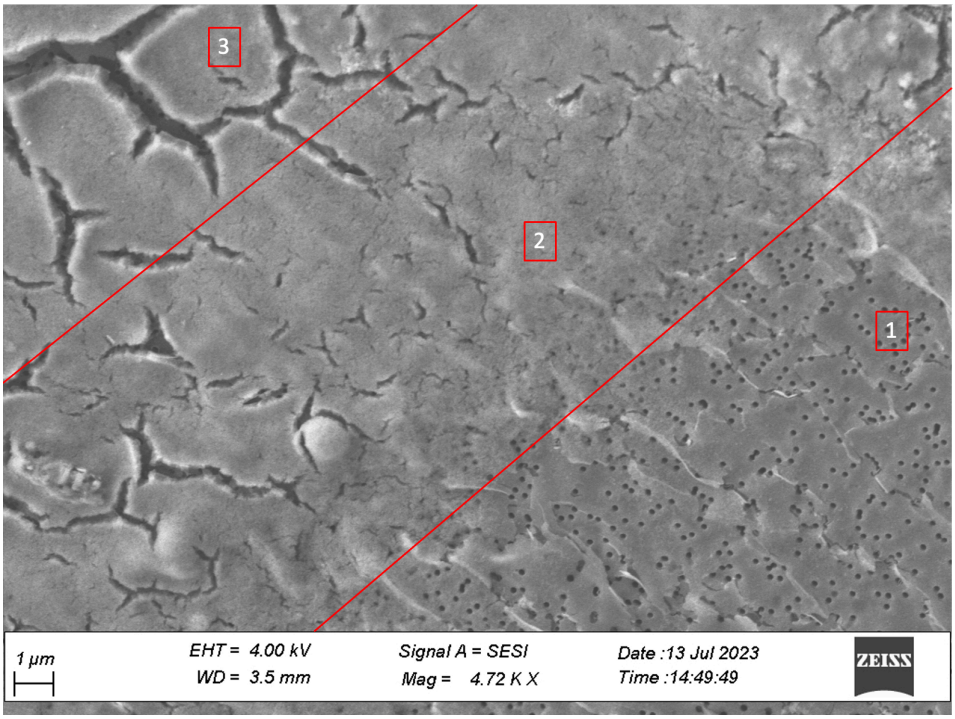

Figure 6.2: SEM image of a PC membrane with a pore size of 150 nm, subjected to 200 ALD cycles of alumina, after use in an electroosmotic pump with DI water. Three different aspects are shown. 1) Normal membrane with visible pores. 2) Clogged pores and crust formation. 3) Crust detachment.

Figure 6.3 shows the same membrane but in a different location. The detachment of the formed crust is clearly visible, as is its back.

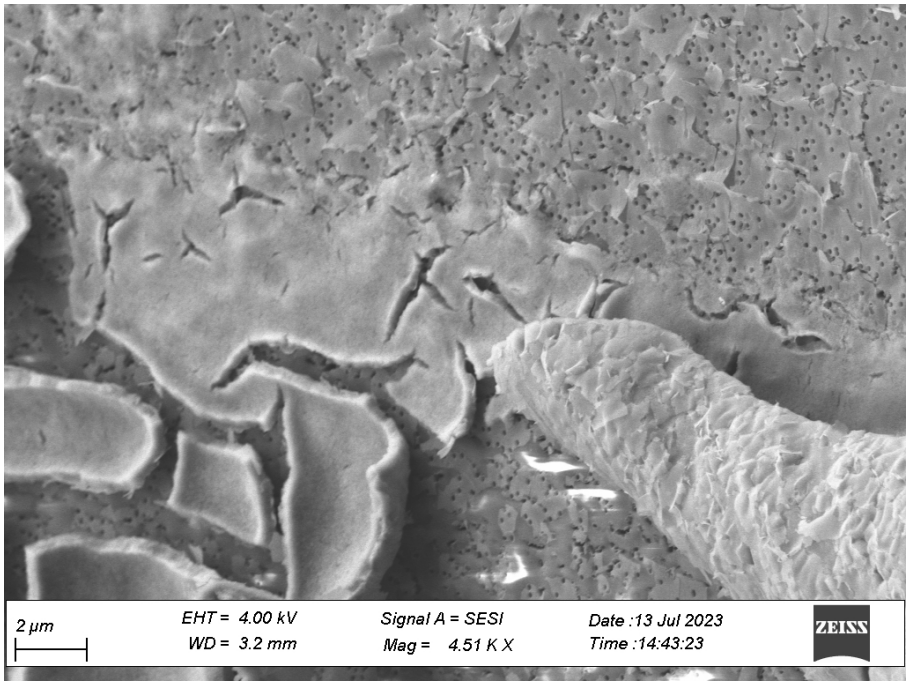

Figure 6.3: SEM image of a PC membrane with a pore size of 150 nm, subjected to 200 ALD cycles of alumina, after use in an electroosmotic pump with DI water. A crust gradually forms, clogging the pores. It can be seen in the bottom right-hand corner of the image, with the back of the crust visible.

The thickness of this layer is between 500 and 1 μm. The thickness of the alumina deposit on top of the membrane is approximately 7.5 nm (due to observed pore reduction). Therefore, this additional crust visible on the SEM images is thicker than the ALD deposit. EDX analysis was carried out to determine the composition of this layer. It turns out that, apart from carbon, oxygen and aluminum, no other elements are present. As polycarbonate is made up of oxygen and carbon (and hydrogen), and alumina is made of aluminum and oxygen, the hypothesis of contamination during ALD deposition is removed. Furthermore, there is around 9 times more aluminium in the crust than in the lower layer, where the pores are visible. Oxygen is also 3.5 times more present in this layer. On the other hand, there is approximately 5 times less carbon in the crust. Therefore, the crust is mainly composed of the alumina deposit.

One possible hypothesis for the observed crust formation is related to the electroosmotic phenomenon. It suggests that during the process, some of the alumina deposited within the pores migrates towards the membrane's surface, where it

agglomerates and eventually detaches.

Considering a uniform deposit of 7.5 nm of alumina in each pore (152 nm in diameter and 47 μm in thickness), an alumina volume of approximately 0.16 μm^3 is present. If this volume were condensed at the membrane's surface, within the pore area, it would have a thickness of about 9 μm. Additionally, as confirmed by the EDX composition analysis, there is still alumina present in the pores, approximately nine times less than what is found in the crust. Therefore, the volume of alumina that could migrate from the pore surface to the membrane surface in the area of the pore is approximately 8.1 μm^3.

Considering the membrane's porosity (12.9%), an even distribution of this volume on the membrane surface would result in a layer of approximately 1 μm. As the thickness of the crust has been determined to be between 500 nm and 1 μm, depending on the place on the membrane, the value obtained corresponds to the maximum possible crust thickness determined from SEM images.

While this hypothesis offers a possible explanation for the origin of the crust, the reasons for its creation and detachment from the membrane remain unclear. It would be very interesting to investigate this phenomenon in future research.

6.4 Influence of time on flow performance

As demonstrated in chapter 5.2, the experimentally obtained flow rate does not consistently reach a steady state for certain membranes. Instead, it exhibits a transient regime, where the flow rate decreases before stabilizing. Surprisingly, no similar phenomenon could be identified in the existing literature. As a result, it is challenging to propose a hypothesis to explain this particular phenomenon.

Nevertheless, a possible lead to follow to explain this phenomenon could be linked to the swelling[2] behavior of the membrane when immersed in water. This phenomemon has the capacity to modify membrane properties as its structure undergoes changes. The time needed for the membrane to normalize after this swelling process might align to the time needed for the flow rate to stabilize.

[2]As mentioned in [64], swelling is defined as "a penetration of a solvent into the polymer network that causes an abrupt change in the volume, moving the boundary from unsolvated glassy region to solvated and expanding rubbery domain".

6.5 Differences between experimental, numerical and analytical results

As can be seen in Figure 5.8, there are differences between the flow rates obtained experimentally, numerically with the Comsol software and analytically using equation 5.1. The numerical resolution gives the best flow rate, followed by the analytical resolution and finally the experiments. Despite these differences in values, all resolutions give the same trend, with flow rate increasing with pore size.

The observed difference in flow could be attributed to certain assumed values used in the flow rate equation and in simulations.

For instance, the pH of deionized water was set at 5 based on literature, but if the actual pH is higher, it would lead to an increase in ion concentrations in the electrolyte, resulting in a larger Debye length. This increase in Debye length would, in turn, elevate the zeta potential, leading to an increase in flow rate.

As discussed in section 6.1.2, the zeta potential varies with pore size, decreasing as the pore radius increases. For polycarbonate, a ζ of -25 mV was assumed from the literature. However, as shown in Figure 6.1, for a pore size of approximately 150 nm, the experimentally obtained zeta potential is -29 mV. Conversely, for a larger pore size of 1.2 μm, ζ decreases to -16 mV. Repeating the simulations with this experimentally obtained ζ value gives a flow rate about 1.5 times lower for the latter membrane. This gives a value closer to the one obtained from experiments. This variation in zeta potential, and therefore in surface charge density, with pore size could be part of the explanation for these differences between experimental and numerical flow resolutions.

Another plausible explanation for the differences in flow rate between resolutions could be attributed to the roughness of the membrane. A completely smooth pore has been assumed in the numerical simulations. Nevertheless, cross-sectional imaging of a polymer membrane revealed that its pores were not perfectly smooth. As explained for the porous silicon, an increase in pore roughness consequently implies a decrease in flow.

Furthermore, as explained in section 5.3, pressure is set to zero in the flow rate equation. Indeed, as the setup is placed horizontally, no pressure gradient due to gravity is applied. As this was done approximately, a pressure gradient may arise experimentally, that is not taken into account in the flow rate analytical resolution.

Moreover, making the hypothesis of no pressure gradient deletes the first term of equation 5.1 for flow rate resolution. This leads to the suppression of thickness as a parameter for flow rate.

CHAPTER 7

CONCLUSION

The study explored parameters influencing surface charge density through investigations involving various materials. This was achieved through both experimental determination of flow rates and numerical simulations using the software Comsol Multiphysics. Firstly, as already observed in literature, surface charge density increases as pore size decreases. This phenomenon is due to pore curvature. Additionally, a comparative analysis of different materials was conducted, ranking them based on their zeta potentials and, consequently, their surface charge densities. The ranking of zeta potentials magnitude in absolute value was found to be $\zeta_{Al_2O_3} > \zeta_{PI} > \zeta_{PC} > \zeta_{PE}$. Finally, this work revealed that experimental flow rate exhibit time-dependent variations. Specifically, an initial transient regime was identified before the flow rate stabilized.

Furthermore, two surface modifications were performed on polycarbonate membranes. The first was a metallization of one side, aiming to halve the electrode distance and theoretically double pump performance. Results shows indeed a increase in flow rate, but not as much as expected. Moreover, it increased more for larger pore size. The second modification was an atomic layer deposition of alumina to reduce pore size. This resulted in a reverse flow direction and an overall increase in flow rate. Furthermore, a particular phenomenon was observed on these membranes with 200 ALD cycles following electroosmotic pumping. Certain areas of the membrane developed a crust containing approximately 90% more alumina content than under it. This phenomenon would be very interesting to investigate in future research.

In this master's thesis, the primary objective was to analytically determine the surface charge density of a nanoporous silica membrane based on experimental measurements of electroosmotic flow rate. However, despite the designed setup, no observable flow could be detected in this particular membrane. More research is therefore needed to fully understand this phenomenon.

APPENDIX

Appendix A: Experimental set-up drawings

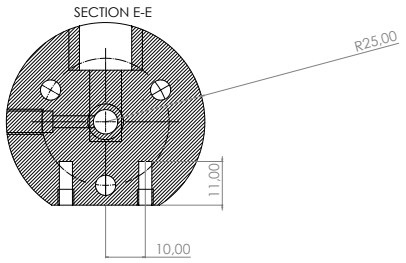

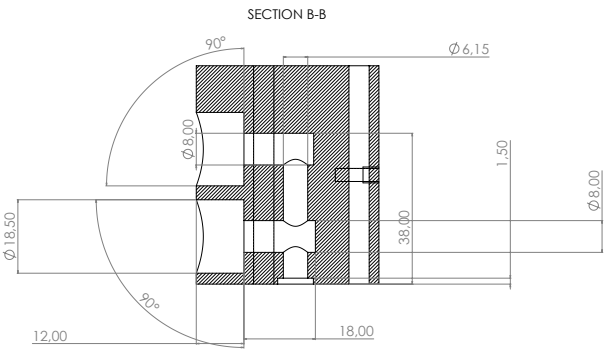

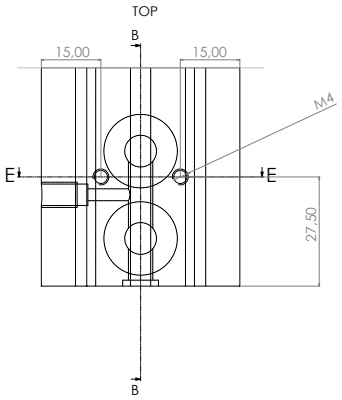

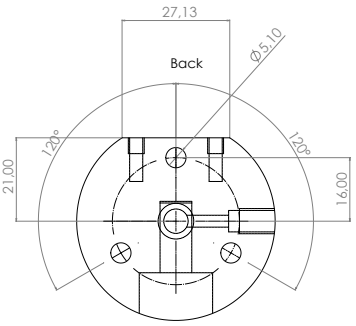

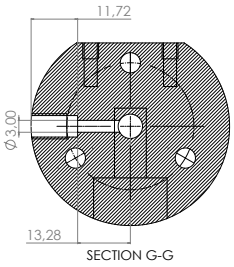

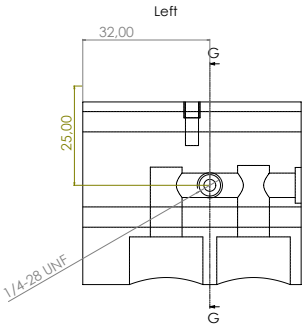

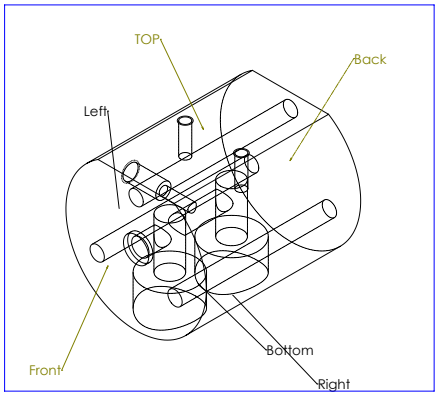

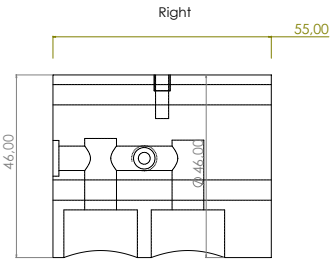

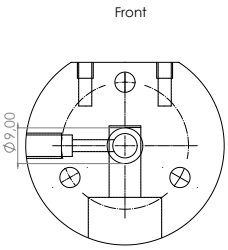

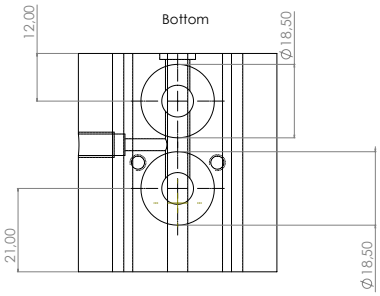

BIBLIOGRAPHY

[1] C. J. C. Biscombe, "The Discovery of Electrokinetic Phenomena: Setting the Record Straight," *Angewandte Chemie*, vol. 56, no. 29, pp. 8338–8340, Nov. 2016.

[2] X. Wang, C. Cheng, S. Wang, and S. Liu, "Electroosmotic pumps and their applications in microfluidic systems," *Microfluidics and nanofluidics*, vol. 6, p. 145, Feb. 2009.

[3] C. He, Z. Zhu, C. Gu, J. Lu, and S. Liu, "Stacking open-capillary electroosmotic pumps in series to boost the pumping pressure to drive high-performance liquid chromatographic separations," *Journal of Chromatography A*, vol. 1227, pp. 253–258, 2012.

[4] A. Chen, J. J. Lu, C. Gu, M. Zhang, K. B. Lynch, and S. Liu, "Combining selection valve and mixing chamber for nanoflow gradient generation: Toward developing a liquid chromatography cartridge coupled with mass spectrometer for protein and peptide analysis," *Analytica Chimica Acta*, vol. 887, pp. 230–236, 2015.

[5] S. Nilsson, P. G. Erlandsson, and N. D. Robinson, "Electroosmotic pumps with frits synthesized from potassium silicate," *PloS one*, vol. 10, no. 12, 2015.

[6] Y. Takamura, H. Onoda, H. Inokuchi, S. Adachi, A. Oki, and Y. Horiike, "Low-voltage electroosmosis pump for stand-alone microfluidics devices," *Electrophoresis*, vol. 24, no. 1-2, pp. 185–192, 2003.

[7] Y. Berrouche and Y. Avenas, "Power electronics cooling of 100 w/cm2 using ac electroosmotic pump," *IEEE transactions on power electronics*, vol. 29, no. 1, pp. 449–454, 2013.

[8] W. Shin, J. M. Lee, R. K. Nagarale, S. J. Shin, and A. Heller, "A miniature, nongassing electroosmotic pump operating at 0.5 v," *Journal of the American Chemical Society*, vol. 133, no. 8, pp. 2374–2377, 2011.

[9] L. Duy Thanh and R. Sprik, "Zeta potential measurement using electroosmosis in porous media," vol. 31, pp. 68–76, Jan. 2015.

[10] *Origin of charge at interfaces: Structure of the electrical double layer.* Berlin, Germany: De Gruyter, May 2015, pp. 17–40.

[11] D. Li, *Electrokinetic Microfluidics and Nanofluidics.* Springer, 2022.

[12] R. T. Sane, in *Encyclopedia of Analytical Science (Second Edition).* Walthm, MA, USA: Elsevier, Jan. 2005, pp. 215–221.

[13] Wikipedia : The free encyclopedia, "Double couche électrique," https://fr.wikipedia.org/w/index.php?title=Double_couche_%C3%A9lectrique&oldid=195403941, Jul. 2022, [Online; accessed 23. Jan. 2023].

[14] J. L. Shohet, "Plasma Science and Engineering," in *Encyclopedia of Physical Science and Technology (Third Edition).* Cambridge, MA, USA: Academic Press, Jan. 2003, pp. 401–423.

[15] J. López-García, J. Horno, and C. Grosse, "Poisson-boltzmann description of the electrical double layer including ion size effects," *Langmuir : the ACS journal of surfaces and colloids*, vol. 27, pp. 13 970–4, Dec. 2011.

[16] A. Alizadeh, W.-L. Hsu, M. Wang, and H. Daiguji, "Electroosmotic flow: From microfluidics to nanofluidics," *Electrophoresis*, vol. 42, no. 7-8, p. 834, Apr. 2021.

[17] F. Mohd Omar, H. Aziz, and S. Stoll, "Nanoparticle properties, behavior, fate in aquatic systems and characterization methods," *Journal of Colloid Science and Biotechnology*, vol. 3, pp. 1–30, Jun. 2014.

[18] P. Hiremath, R. S, P. Binnal, and T. Theodore, *Fluoride contamination in underground water and its treatment*, Jan. 2021, pp. 249–280.

[19] R. Hatsuki, F. Yujiro, and T. Yamamoto, "Direct measurement of electric double layer in a nanochannel by electrical impedance spectroscopy," *Microfluids and Nanofluidics*, vol. 14, no. 6, pp. 983–988, Jun. 2013.

[20] R. Peng and D. Li, "Electrokinetic motion of single nanoparticles in single PDMS nanochannels," *Microfluidics and Nanofluidics*, vol. 21, no. 1, Jan. 2017.

[21] E. X. Pérez, "Desing, fabrication and characterization of porous silicon multilayer optical devices," Ph.D. dissertation, Universitat Rovira I Virgili, 2007.

[22] S. Arshavsky-Graham, N. Massad-Ivanir, E. Segal, and S. Weiss, "Porous silicon-based photonic biosensors: current status and emerging applications," *Analytical Chemistry*, vol. 91, no. 1, pp. 441–467, Jan. 2019.

[23] M. J. Sailor, *Porous silicon in practice: preparation, characterization and applications*. Wiley-VCH Verlag GmbH Co. KGaA., 2012.

[24] K. Lin, Z. Li, Y. Tao, K. Li, H. Yang, J. Ma, T. Li, J. Sha, and Y. Chen, "Surface charge density inside a silicon nitride nanopore," *Langmuir*, vol. 37, Sep. 2021.

[25] S. Yao, A. Myers, J. Posner, K. Rose, and J. Santiago, "Electroosmotic pumps fabricated from porous silicon membranes," *Microelectromechanical Systems, Journal of*, vol. 15, pp. 717 – 728, Jul. 2006.

[26] J. Wallner, N. Nagar, C. Friedrich, and P. Bergstrom, "Macro porous silicon as pump media for electro-osmotic pumps," *Physica status solidi (a)*, vol. 204, pp. 1327 – 1331, May 2007.

[27] J. L. Snyder, J. Getpreecharsawas, D. Z. Fang, T. R. Gaborski, C. C. Striemer, P. M. Fauchet, D. A. Borkholder, and J. L. McGrath, "High-performance, low-voltage electroosmotic pumps with molecularly thin silicon nanomembranes," *Proceedings of the National Academy of Sciences of the United States of America*, vol. 110, no. 46, pp. 18 425–18 430, Nov. 2013.

[28] Q. Yang, B. Su, Y. Wang, and W. Wu, "Low-voltage efficient electroosmotic pumps with ultrathin silica nanoporous membrane," *Electrophoresis*, vol. 40, no. 16-17, pp. 2149–2156, Mar. 2019.

[29] Y.-R. Shi, M.-P. Ye, L.-C. Du, and Y.-X. Weng, "Experimental determination of particle size-dependent surface charge density for silica nanospheres," *The Journal of Physical Chemistry C*, vol. 122, no. 41, pp. 23 764–23 771, Oct. 2018.

[30] Y. Li-Hsien, X. Song, W. J. Sang, Q. Shizhi, , and H. Jyh-Ping, "Field effect control of surface charge property and electroosmotic flow in nanofluidics," *The journal of physical chemistry*, vol. 116, p. 4209—4216, 2012.

[31] Y. Jie, S. Haiping, L. Cheng, S. Yazhuo, L. Honglai, and W. Jianzhong, "Understanding surface charge regulation in silica nanopores," *Royal Society of Chemistry*, vol. 22, Jun. 2020.

[32] B. Murat, A. Selcuk, B. Ali, and Q. Shizhi, "Size dependent surface charge properties of silica nanoparticles," *The Journal of Physical Chemistry C*, vol. 118, p. 1836−1842, Jan. 2014.

[33] C. Wang, D. Kong, Q. Chen, and J. Xue, "Surface engineering of synthetic nanopores by atomic layer deposition and their applications," *Frontiers of Materials Science*, vol. 7, Sep. 2013.

[34] A. Thormann, L. Berthold, P. Goring, M. Lelonek, and A. Heilmann, "Nanoporous aluminum oxide membranes for separation and biofunctionalization," *Procedia Engineering*, vol. 44, pp. 1107–1111, Jan. 2012.

[35] S. Inoue, S.-Z. Kure-Chu, K. Wada, D. Li, and H. Haneda, "New roots to formation of nanostructures on glass surface through anodic oxidation of sputtered aluminum," *Science and Technology of Advanced Materials*, vol. 4, pp. 269–276, Jul. 2003.

[36] B. de la Mora and E. Lugo, *Porous silicon biosensors*, Jan. 2013, pp. 141–171.

[37] J. Schmidt, B. Veith-Wolf, F. Werner, D. Zielke, and R. Brendel, "Silicon surface passivation by ultrathin Al2O3 films and Al2O3/SiNx stacks," Jul. 2010, pp. 885 – 890.

[38] M. Becker and M. Sierka, "Atomistic Simulations of Plasma-Enhanced Atomic Layer Deposition," *Materials*, vol. 12, no. 16, p. 2605, Aug. 2019.

[39] D. Gu, S. Yalcin, H. Baumgart, S. Qian, O. Baysal, and A. Beskok, "Electrophoretic light scattering for surface zeta potential measurement of ALD metal oxide films," *ECS Transactions*, vol. 33, no. 2, p. 37, Oct. 2010.

[40] J. Jannsens, "Etude du micro-pompage électro-osmotique de membranes polymères micro-poreuses," Master's thesis, UCLouvain, June 2012.

[41] SciMed, "A brief introduction to SEM (Scanning Electron Microscopy)," https://www.scimed.co.uk/education/sem-scanning-electron-microscopy, Jun. 2023, [Online; accessed 6. Jun. 2023].

[42] A. Ismail, K. Khulbe, and T. Matsuura, *RO Membrane Characterization*, Jan. 2019, pp. 57–90.

[43] ImageJ, "Particle Analysis," https://imagej.net/imaging/particle-analysis, Jun. 2023, [Online; accessed 6. Jun. 2023].

[44] ——, "Analyze Menu," https://imagej.nih.gov/ij/docs/menus/analyze.html, May 2017, [Online; accessed 6. Jun. 2023].

[45] Y.-F. Chen, M.-C. Li, Y.-H. Hu, W.-J. Chang, and C.-C. Wang, "Low-voltage electroosmotic pumping using porous anodic alumina membranes," *Microfluidics and Nanofluidics*, vol. 5, pp. 235–244, Aug. 2008.

[46] Y. Berrouche, "Etude théorique et expérimentale de pompes électro-osmotiques et de leur utilisation dans une boucle de refroidissement de l'électronique de puissance," Ph.D. dissertation, Majmaah University, 2008.

[47] C. R. Buie, J. D. Posner, T. Fabian, S.-W. Cha, D. Kim, F. B. Prinz, J. K. Eaton, and J. G. Santiago, "Water management in proton exchange membrane fuel cells using integrated electroosmotic pumping," *J. Power Sources*, vol. 161, no. 1, pp. 191–202, Oct. 2006.

[48] S. Yao and J. G. Santiago, "Porous glass electroosmotic pumps: theory," *J. Colloid Interface Sci.*, vol. 268, no. 1, pp. 133–142, Dec. 2003.

[49] S. Vishnu and M. Ajith C, "Mathematical modeling of electroosmotic flow through a slit microchannel under the influence of time varying electric field," *International Journal of Mechanical Engineering and Robotics Research*, vol. 3, no. 4, Oct. 2014.

[50] S. Zeng, C.-H. Chen, J. Jr, and J. Santiago, "Fabrication and characterization of electrokinetic micro pumps," vol. 2, Feb. 2000, pp. 31 – 36.

[51] "Table of Diffusion Coefficients," https://www.aqion.de/site/diffusion-coefficients, Jul. 2023, [Online; accessed 19. Jul. 2023].

[52] "Deionized water," https://www.chemeurope.com/en/encyclopedia/Deionized_water.html?fbclid=IwAR0lRgtZpC31GUKZ0lTuharlE-SMn5Tkr9WtAl_iC0UW9I5J8Z-r9GP2GFo, Jul. 2023, [Online; accessed 20. Jul. 2023].

[53] C. Wang, L. Wang, X. Zhu, Y. Wang, and J. Xue, "Low-voltage electroosmotic pumps fabricated from track-etched polymer membranes," *Lab on a chip*, vol. 12, pp. 1710–6, Mar. 2012.

[54] I.-K. Jun and H. Hess, "A biomimetic, self-pumping membrane," *Adv. Mater.*, vol. 22, no. 43, pp. 4823–4825, Nov. 2010.

[55] B. Kirby and E. Hasselbrink, "Zeta potential of microfluidic substrates: 2. data for polymers," *Electrophoresis*, vol. 25, pp. 203–13, Jan. 2004.

[56] Z. Kolská, Z. Makajova, K. Kolarova, N. Slepičková, S. Trostova, A. Reznickova, J. Siegel, and V. Svorcik, "Electrokinetic potential and other surface properties of polymer foils and their modifications," *Polymer Science*, pp. 203–228, Jan. 2013.

[57] T. Luxbacher, "Electrokinetics on polymer surfaces: The zeta potential as an indicator for swelling and adsorption processes," pp. 74–78, Mar. 2010.

[58] K. Gopalu, S. Rangaraj, R. Venkatachalam, and N. Kannan, "Effect of contact angle, zeta potential and particles size on the in vitro studies of Al2O3 and SiO2 nanoparticles," *IET nanobiotechnology*, vol. 9, pp. 27–34, Feb. 2015.

[59] A. Sayano, T. Shiota, A. Nishiyama, K. Yasuda, and K. Shinozaki, "Apparent zeta potential of nano-porous Al2O3 film deposited on different substrates in streaming potential method," *Journal of Materials Science*, vol. 53, Dec. 2018.

[60] P. Xu, H. Wang, R. Tong, Q. Du, and W. Zhong, "Preparation and morphology of SiO2/PMMA nanohybrids by microemulsion polymerization," *Colloid and Polymer Science*, vol. 284, pp. 755–762, Apr. 2006.

[61] S. McInnes, C. Turner, S. Al-Bataineh, M. Airaghi Leccardi, Y. Irani, A. Cowin, K. Williams, and N. Voelcker, "Surface engineering of porous silicon to optimise therapeutic antibody loading and release," *Journal of Materials Chemistry B*, vol. 3, May 2015.

[62] Z. Xia, V. Rozyyev, A. Mane, J. Elam, and S. Darling, "Surface zeta potential of ald-grown metal-oxide films," *Langmuir*, vol. 37, Sep. 2021.

[63] F. Li, Y. Yang, Y. Fan, W. Xing, and Y. Wang, "Modification of ceramic membranes for pore structure tailoring: The atomic layer deposition route," *Journal of Membrane Science*, vol. 397–398, p. 17 – 23, Apr. 2012.

[64] A. Gugliuzza, "Solvent Swollen Polymer," in *Encyclopedia of Membranes*. Berlin, Germany: Springer, Aug. 2016, pp. 1801–1802.

About the use of AI

This work relies on AI to improve its presentation. In practice, Deepl has been used for some translations. ChatGPT was also used throughout the writing process of this thesis to help reformulate and proofread some of the paragraphs I wrote.

UNIVERSITÉ CATHOLIQUE DE LOUVAIN
École polytechnique de Louvain
Rue Archimède, 1 bte L6.11.01, 1348 Louvain-la-Neuve, Belgique | **www.uclouvain.be/epl**